THE ASTROPHYSICAL JOURNAL, 785:75 (26pp), 2014 April 10 doi:10.1088/0004-637X/785/1/75

THE SINS/zC-SINF SURVEY OF $z \sim 2$ GALAXY KINEMATICS: EVIDENCE FOR GRAVITATIONAL QUENCHING*

R. GENZEL[1,2,3], N. M. FÖRSTER SCHREIBER[1], P. LANG[1], S. TACCHELLA[4], L. J. TACCONI[1], S. WUYTS[1], K. BANDARA[1], A. BURKERT[1,5], P. BUSCHKAMP[1], C. M. CAROLLO[4], G. CRESCI[6], R. DAVIES[1], F. EISENHAUER[1], E. K. S. HICKS[7], J. KURK[1], S. J. LILLY[4], D. LUTZ[1], C. MANCINI[8], T. NAAB[9], S. NEWMAN[3], Y. PENG[4,10], A. RENZINI[8], K. SHAPIRO GRIFFIN[11], A. STERNBERG[12], D. VERGANI[13], E. WISNIOSKI[1], E. WUYTS[1], AND G. ZAMORANI[14]

[1] Max-Planck-Institut für Extraterrestrische Physik (MPE), Giessenbachstr.1, D-85748 Garching, Germany; genzel@mpe.mpg.de
[2] Department of Physics, Le Conte Hall, University of California, Berkeley, CA 94720, USA
[3] Department of Astronomy, Campbell Hall, University of California, Berkeley, CA 94720, USA
[4] Institute for Astronomy, Department of Physics, Eidgenössische Technische Hochschule, ETH Zürich, 8093-CH, Switzerland
[5] Universitäts-Sternwarte Ludwig-Maximilians-Universität (USM), Scheinerstr. 1, D-81679 München, Germany
[6] Istituto Nazionale di Astrofisica—Osservatorio Astronomico di Arcetri, Largo Enrico Fermi 5, I-50125 Firenze, Italy
[7] Department of Physics and Astronomy, University of Alaska Anchorage, 3211 Providence Drive, Anchorage, AK 99507, USA
[8] Osservatorio Astronomico di Padova, Vicolo dell'Osservatorio 5, I-35122 Padova, Italy
[9] Max-Planck Institute for Astrophysics, Karl Schwarzschildstrasse 1, D-85748 Garching, Germany
[10] Cavendish Laboratory, Room 908 Rutherford Building, J. J. Thomson Avenue, Cambridge CB3 0HE, UK
[11] Space Sciences Research Group, Northrop Grumman Aerospace Systems, Redondo Beach, CA 90278, USA
[12] School of Physics and Astronomy, Tel Aviv University, Tel Aviv 69978, Israel
[13] INAF Istituto di Astrofisica Spaziale e Fisica Cosmica di Bologna, Via P. Gobetti 101, I-40129 Bologna, Italy
[14] INAF Osservatorio Astronomico di Bologna, Via Ranzani 1, I-40127 Bologna, Italy
Received 2013 October 10; accepted 2014 February 22; published 2014 March 27

ABSTRACT

As part of the SINS/zC-SINF surveys of high-z galaxy kinematics, we derive the radial distributions of Hα surface brightness, stellar mass surface density, and dynamical mass at $\sim$2 kpc resolution in 19 $z \sim 2$ star-forming disks with deep SINFONI adaptive optics spectroscopy at the ESO Very Large Telescope. From these data we infer the radial distribution of the Toomre Q-parameter for these main-sequence star-forming galaxies (SFGs), covering almost two decades of stellar mass ($10^{9.6}$–$10^{11.5}\,M_\odot$). In more than half of our SFGs, the Hα distributions cannot be fit by a centrally peaked distribution, such as an exponential, but are better described by a ring, or the combination of a ring and an exponential. At the same time the kinematic data indicate the presence of a mass distribution more centrally concentrated than a single exponential distribution for 5 of the 19 galaxies. The resulting Q-distributions are centrally peaked for all, and significantly exceed unity there for three-quarters of the SFGs. The occurrence of Hα rings and of large nuclear Q-values appears to be more common for the more massive SFGs. While our sample is small and biased to larger SFGs, and there remain uncertainties and caveats, our observations are consistent with a scenario in which cloud fragmentation and global star formation are secularly suppressed in gas-rich high-z disks from the inside out, as the central stellar mass density of the disks grows.

Key words: cosmology: observations – galaxies: evolution – galaxies: high-redshift – infrared: galaxies

Online-only material: color figures

1. INTRODUCTION AND THEORETICAL BACKGROUND

Look-back studies have shown that most of the "normal," massive star-forming galaxies (SFGs) from $z \sim 0$ to $z \sim 2.5$ are located on or near a star formation "main sequence" in the stellar mass (M_*)–star formation rate (SFR) plane, whose slope is near-universal (SFR $\sim M_*^{0.7-1}$) but whose amplitude, the specific star formation rate (sSFR = SFR/M_*), strongly changes with cosmic epoch (sSFR $\sim (1+z)^{2.9}$; Daddi et al. 2007; Noeske et al. 2007; Schiminovich et al. 2007; Rodighiero et al. 2010, 2011; Whitaker et al. 2012). As a result, the stellar buildup at early times is largely due to intrinsic star formation along the main sequence.

The ionized gas kinematics of these SFGs (Genzel et al. 2006, 2008; Förster Schreiber et al. 2006, 2009, 2013; Stark et al. 2008; Wright et al. 2009; Law et al. 2009; Puech 2010; Jones et al. 2010; Epinat et al. 2012; Vergani et al. 2012; Wisnioski et al. 2012; Swinbank et al. 2012; Newman et al. 2013), as well as their rest-frame optical/UV brightness distributions (Wuyts et al. 2011a), suggest that 30%–70% of the massive ($\log M_*$ $(M_\odot) > 9.5$) main-sequence SFGs to $z \sim 2.5$ are rotationally supported disks, albeit with large velocity dispersions, frequent perturbations due to minor mergers, and highly clumpy and irregular appearances in UV/optical broadband imagery (Cowie et al. 1995; van den Bergh et al. 1996; Giavalisco et al. 1996; Elmegreen et al. 2004, 2009; Förster Schreiber et al. 2009, 2011a, 2011b).

The first systematic studies of molecular gas in main-sequence SFGs from $z \sim 0$ to $z \sim 3$ find that the evolution of sSFRs above can be accounted for by corresponding changes in the molecular gas reservoirs, combined with a slowly changing depletion timescale of molecular gas to stars ($t_{\rm depletion} = M_{\rm mol\ gas}/{\rm SFR} \sim t_0 \times (1+z)^{-\beta}$, with $t_0 \sim 1.5 \pm 0.4$ Gyr and $\beta \sim 1 \pm 0.4$; Tacconi et al. 2010, 2013; Genzel et al. 2010;

* Based on observations obtained at the Very Large Telescope of the European Southern Observatory, Paranal, Chile (ESO program IDs 076.A-0527, 079.A-0341, 080.A-0330, 080.A-0339, 080.A-0635, 081.A-0672, 082.A-0396, 183.A-0781, 087.A-0081, 088.A-0202, 088.A-0202, 088.A-0209, 091.A-0126). Also based on observations made with the NASA/ESA *Hubble Space Telescope*, obtained at the Space Telescope Science Institute, which is operated by the Association of Universities for Research in Astronomy, Inc., under NASA contract NAS 5-26555 (GO programs Nos. 10924 and 12587).

Daddi et al. 2010a, 2010b; Saintonge et al. 2011, 2012, 2013; Bauermeister et al. 2013). High-z SFGs form stars rapidly, mainly because they are gas rich and globally unstable in their entire disks to gravitational fragmentation and star formation (Genzel et al. 2011).

These basic observational findings can be understood in a simple physical framework, in which global ("violent") gravitational instability and fragmentation in quasi-steadily fed, gas-rich disks create large, massive star-forming clumps, which in turn drive turbulence through gravitational torques and stellar feedback (Noguchi 1999; Immeli et al. 2004a, 2004b; Bournaud et al. 2007; Elmegreen et al. 2008; Genzel et al. 2008; Elmegreen 2009; Dekel et al. 2009a, 2009b; Bournaud 2010; Cacciato et al. 2012; Forbes et al. 2013). The most recent generation of cosmological galaxy evolution models and simulations find that the buildup of $z > 1$ SFGs is dominated by smooth accretion of gas and/or minor mergers, and that stellar buildup at early times is largely due to in situ star formation (Kereš et al. 2005, 2009; Dekel & Birnboim 2006; Bower et al. 2006; Kitzbichler & White 2007; Ocvirk et al. 2008; Guo & White 2008; Dekel et al. 2009a; Davé et al. 2011, 2012). The large and quasi-steady gas accretion may plausibly build up early galaxy disks with a mass doubling timescale of ~0.5 Gyr at $z \sim 2$ (Dekel et al. 2009a; Agertz et al. 2009; Brooks et al. 2009; Ceverino et al. 2010). If the incoming material is gas rich, then global gravitational instabilities in these disks plausibly account for the large gas fractions and the star formation main-sequence evolution inferred from the observations (Genel et al. 2008; Dekel et al. 2009b; Bouché et al. 2010; Davé et al. 2012; Lilly et al. 2013; Hirschmann et al. 2013).

Bulge formation in these early disks has traditionally been thought to occur in major mergers (e.g., Kauffmann & Haehnelt 2000; Di Matteo et al. 2005). The gravitational disk instability in early gas-rich disks may open a second channel for bulge formation through internal radial gas transport. Star-forming clumps and distributed gas in the disk are expected to migrate into the center via dynamical friction, viscosity, and tidal torques, on a timescale of

$$t_{\rm inspiral} \approx (v_c/\sigma_0)^2 t_{\rm dyn}(R_{\rm disk}) \sim 10 t_{\rm dyn}(R_{\rm disk}) \sim t_{\rm orb}(R_{\rm disk}) < 0.5\,{\rm Gyr}, \quad (1)$$

where $t_{\rm dyn} = R_{\rm disk}/v_c$ and $t_{\rm orb} = 2\pi t_{\rm dyn}$ are the mean disk dynamical and orbital timescales, respectively. The inspiraling gas/stars may form a central bulge, and perhaps also a central massive black hole and a remnant thick disk (Noguchi 1999; Immeli et al. 2004a, 2004b; Förster Schreiber et al. 2006; Genzel et al. 2006, 2008; Elmegreen et al. 2008; Carollo et al. 2007; Dekel et al. 2009b; Bournaud et al. 2009; Ceverino et al. 2010). Inward radial transport depends strongly on v_c/σ_0. Importantly, since high-z disks are turbulent, the radial transport timescales are significantly smaller than the Hubble and gas depletion times and are comparable to the orbital and mass-doubling timescales. In simulations the rate of mass inflow into the central region is comparable to the SFR in the disk (Dekel et al. 2013). The internal radial transport also redistributes angular momentum, resulting in higher angular momentum outer disks, relative to the inner stellar component, consistent with recent observations (Nelson et al. 2012, 2013).

A rotating, symmetric and thin *gas* disk is unstable to gravitational fragmentation if the Toomre Q-parameter (Toomre 1964) is below a critical value $Q_{\rm crit}$. For a thin gas-dominated disk in a background potential (of dark matter and an old stellar component) Q is related to the local gas velocity dispersion σ_0 (assuming isotropy), circular velocity v_c, epicyclic frequency κ ($\kappa^2 = 2(v_c/R)^2 + (v_c/R)\, dv_c/dR$), and gas surface density $\Sigma_{\rm gas}$ at radius R via the relation (Wang & Silk 1994; Binney & Tremaine 2008; Escala & Larson 2008; Elmegreen 2009; Dekel et al. 2009b; Cacciato et al. 2012)

$$Q_{\rm gas} = \frac{\kappa(R)\sigma_0(R)}{\pi G \Sigma_{\rm gas}(R)}. \quad (2)$$

In the single-component case $Q_{\rm crit} \sim 1$. For a thick disk the surface gravity in the z-direction is lowered and the critical Q drops to $Q_{\rm crit} \sim 0.67$ (Goldreich & Lynden-Bell 1965). The situation for multi-component thin or thick disks is more complicated and depends on the Q-values of the individual components, as well as their velocity dispersions (Cacciato et al. 2012; Romeo & Falstad 2013). If the disk consists of molecular (H$_2$+He), atomic (H I+He), and stellar (*) components, $Q_{\rm tot}{}^{-1} = Q_{\rm H2}{}^{-1} + Q_{\rm HI}{}^{-1} + Q_*{}^{-1}$ if all components have similar velocity dispersions, thus increasing the Q-thresholds for the individual components for the combined system to become critical. So for a thin disk of molecular gas and stars with the same $Q = Q_* = Q_{\rm gas}$, the critical $Q_{\rm gas}$ in the combined system becomes $Q_{\rm crit,gas} \sim 2$. For a two-component thick disk $Q_{\rm crit,gas} \sim 1.32$.

Assuming that thick, high-z disks thermostat at marginal (in)stability, $Q \sim Q_{\rm crit} \sim 0.67$–$1.3$, one finds from Equation (2) with $\kappa = a\, v_c/R$

$$Q = \frac{a v_c \sigma_0}{\pi R G \Sigma_{\rm gas}} = a \times \frac{v_c^2 R/G}{\pi R^2 \Sigma_{\rm gas}} \times \frac{\sigma_0}{v_c} = \frac{a}{f_{\rm gas}} \times \frac{\sigma_0}{v_c}, \quad (3)$$

where a ranges from 1 (for a Keplerian rotation curve), 1.4 (for a flat rotation curve), to 2 (for a solid-body rotation curve) and $f_{\rm gas}$ is the fraction of gas to the total mass in the disk (Genzel et al. 2008, 2011; Dekel et al. 2009b). For $Q \sim 1$, $\sigma_0/v_c = f_{\rm gas}/a$. This result and Equation (1) show that the disk instability mechanism drives gas inward rapidly when the gas fraction is high, which is the case at $z \sim 1$–3 but increasingly less so at lower redshifts.

If the radial gas transport discussed above builds up the central (mainly stellar) mass over a number of orbital timescales, and simultaneously the gas accretion rate into the disk slowly drops over cosmic time, or because the halo mass grows above $10^{11.6}$–$10^{12}\, M_\odot$ (Rees & Ostriker 1977; Dekel & Birnboim 2006; Ocvirk et al. 2008; Dekel et al. 2009a), there should come a phase, depending on the efficacy of stellar feedback and radial gas transport, when Q in the central disk exceeds the critical value due to rotational shear (Hunter et al. 1998). The gravitational fragmentation process and the global disk instability may then shut off. This "morphological" or "gravitational" quenching mechanism (Martig et al. 2009, 2013) by itself cannot result in a permanent shutdown of star formation in the central disk, as long as gas is accumulating there due to radial transport. Either the radial transport into the center has to cease, or the accumulating but sterile gas needs to be removed, for instance, by stellar or active galactic nucleus (AGN) feedback. Even if the gravitational quenching mechanism operates and the global Q exceeds the critical value, star formation may still occur in localized regions where dense, gravitationally bound clouds or cores form (see Section 3.6). In essence gravitational quenching reduces the efficiency of star formation and increases the molecular gas depletion timescale in the central parts of the disk. The global disk instability may also be rekindled if a large fluctuation occurs in external gas accretion, for instance, as a result of a merger. However, conceptually gravitational quenching in combination with efficient feedback may provide a powerful process that could shut down global disk instability secularly, from the inside out (Martig et al. 2009). Indeed, recent simulations and semi-analytic models confirm that this process may play an important role in stabilizing disks, especially at late times.

In this paper we take advantage of the unique, high-quality SINS/zC-SINF sample of $z \sim 1.5$–2.5 SFGs presented in N. M. Förster Schreiber et al. (2014, in preparation, henceforth FS14), along with ancillary *Hubble Space Telescope* (*HST*) WFC3 near-infared imaging by S. Tacchella et al. (in preparation) of the majority of the same galaxies, in order to test for evidence of the gravitational shutdown process discussed above. The SINS/zC-SINF sample provides deep, adaptive optics (AO) assisted SINFONI/Very Large Telescope (VLT) integral field unit (IFU) spectroscopy (Eisenhauer et al. 2003; Bonnet et al. 2004) of 35 $z = 1.5$–2.5 SFGs. With these data it is now possible, for the first time, to derive significant constraints on the radial and mass variation of the Q-parameter in a statistically meaningful sample of massive high-z SFGs. We adopt a ΛCDM cosmology with $\Omega_m = 0.27$, $\Omega_b = 0.046$, and $H_0 = 70$ km s^{-1} Mpc^{-1} (Komatsu et al. 2011), as well as a Chabrier (2003) initial stellar mass function (IMF).

2. OBSERVATIONS AND ANALYSIS

2.1. Galaxy Sample

We have selected our galaxies from the AO assisted Hα IFU sample of FS14 (see also Förster Schreiber et al. 2009; Mancini et al. 2011), which in turn is drawn from several color- and/or magnitude-selected, rest-frame optical/UV imaging samples, with ground-based optical spectroscopic redshift identifications. We refer to the above papers for all details on the observations, data reduction, and spectral/spatial analysis. The 35 $z \sim 1.5$–2.5 SFGs in FS14 are broadly representative of the overall near-main-sequence, rest-optical/UV-selected star-forming population over the stellar mass range $\log M_* = 9.2$–11.5. They are somewhat biased toward bluer and more actively star-forming objects, largely because of the necessary (rest-UV) spectroscopic redshifts and the need for relatively high Hα surface brightness at least over some parts of the galaxies for detailed AO IFU follow-up (FS14).

From these 35 AO data sets (with a typical angular resolution of FWHM $\sim 0\farcs2$, and spectral resolution of 85 km s^{-1} in K band and 120 km s^{-1} in H band) we selected rotation-dominated galaxies, with

1. a smooth, continuous velocity gradient along the morphological major axis, and with no abrupt velocity jumps in the outer parts of the galaxy that might be indicative of a (major) merger. In most cases the projected velocity along the major axis levels off to an asymptotic value in the outer parts of the galaxy, as expected for a flat outer rotation curve;
2. a projected velocity dispersion distribution peaking on/near the kinematic center, in many cases also identical with the center/nucleus of the galaxy on the ancillary *HST* images;
3. a sufficiently large size and signal-to-noise ratio per pixel to constrain the radial velocity distribution for dynamical modeling.

These criteria are necessary requirements if the large-scale velocity field of the galaxy is to be dominated by rotation. They may not be sufficient to screen against minor mergers or out of equilibrium disks formed in the aftermath of a major merger (see Robertson et al. 2006; Robertson & Bullock 2008). With these selections, our sample retains 19 of the 35 SFGs in FS14.

We investigated whether the structural properties as measured in the rest-frame optical light of the SINS/zC-SINF galaxies in our sample are representative of those of the underlying population. To this end, we drew for each galaxy in our sample 40 galaxies at random with similar mass, SFR, and redshift from CANDELS, a large and unbiased *HST* imaging survey (Grogin et al. 2011; Koekemoer et al. 2011). Quantifying the structure of SINS/zC-SINF and matched CANDELS galaxies following identical procedures and based on the observed H-band surface brightness distributions, a Kolmogorov–Smirnov test shows no significant difference in the distribution of Sérsic indices, while the size distribution is significantly different, at the 99% confidence level. The median/mean Sérsic index of our sample is $\sim$1, in agreement with the mean of the main-sequence population (Wuyts et al. 2011a). The galaxies in our sample are in the median a factor 1.6 larger than their matched CANDELS counterparts. As described above, this is an inevitable consequence of our wanting to derive spatially well-resolved kinematics with a resolution of $\sim 0\farcs2$–$0\farcs3$ (corresponding to $\sim$2 kpc), and thus having to exclude the smaller systems in the FS14 AO sample. However, Newman et al. (2013) have shown that most of these smaller, "dispersion dominated" SFGs likely are rotating disks as well, albeit with a smaller ratio of rotation to local velocity dispersion.

It is important to point out that the structural parameters of clumpy systems, such as many in our sample, move on average to lower Sérsic indices and larger sizes if the center is fixed at the dynamical center, rather than left as a free parameter, as is the practice in most studies of galaxy structure. Running GALFIT with the center of our galaxies fixed to the dynamical center would somewhat increase the difference in Sérsic index and size distribution with respect to the CANDELS control sample, for which no dynamical information is available.

Figure 1 shows the integrated narrow-line Hα maps (extracted as described in point d below) for all 19 SFGs discussed in this paper, and arranged in the stellar mass–SFR plane. Table 1 lists their salient properties. The diagonal continuous and dotted, white lines in Figure 1 mark the location of the $z \sim 2$ main sequence (assumed to have unity slope), as well as SFRs four times above and below. The dotted lines thus approximately denote the scatter around the main sequence (Noeske et al. 2007). The 19 SFGs cover quite well the overall main-sequence population over almost a factor of 100 in stellar mass, also reflecting the same modest bias toward above main-sequence galaxies, especially at lower masses, as in the overall SINS/zC-SINF survey (Förster Schreiber et al. 2009, 2013; Mancini et al. 2011).

2.2. Kinematic and Mass Modeling

As discussed previously in Genzel et al. (2011), our kinematic analysis and modeling incorporate the following steps:

1. *Extraction of observed spectra*. We extracted spectra along the structural/kinematic major axis using a synthetic slit passing through the kinematic center, with an effective sampling of $0\farcs1$–$0\farcs2$ along the slit, and a width of $0\farcs25$–$0\farcs3$ perpendicular to the slit. Gaussian fits deliver Hα surface brightness I, projected velocity v, and projected velocity

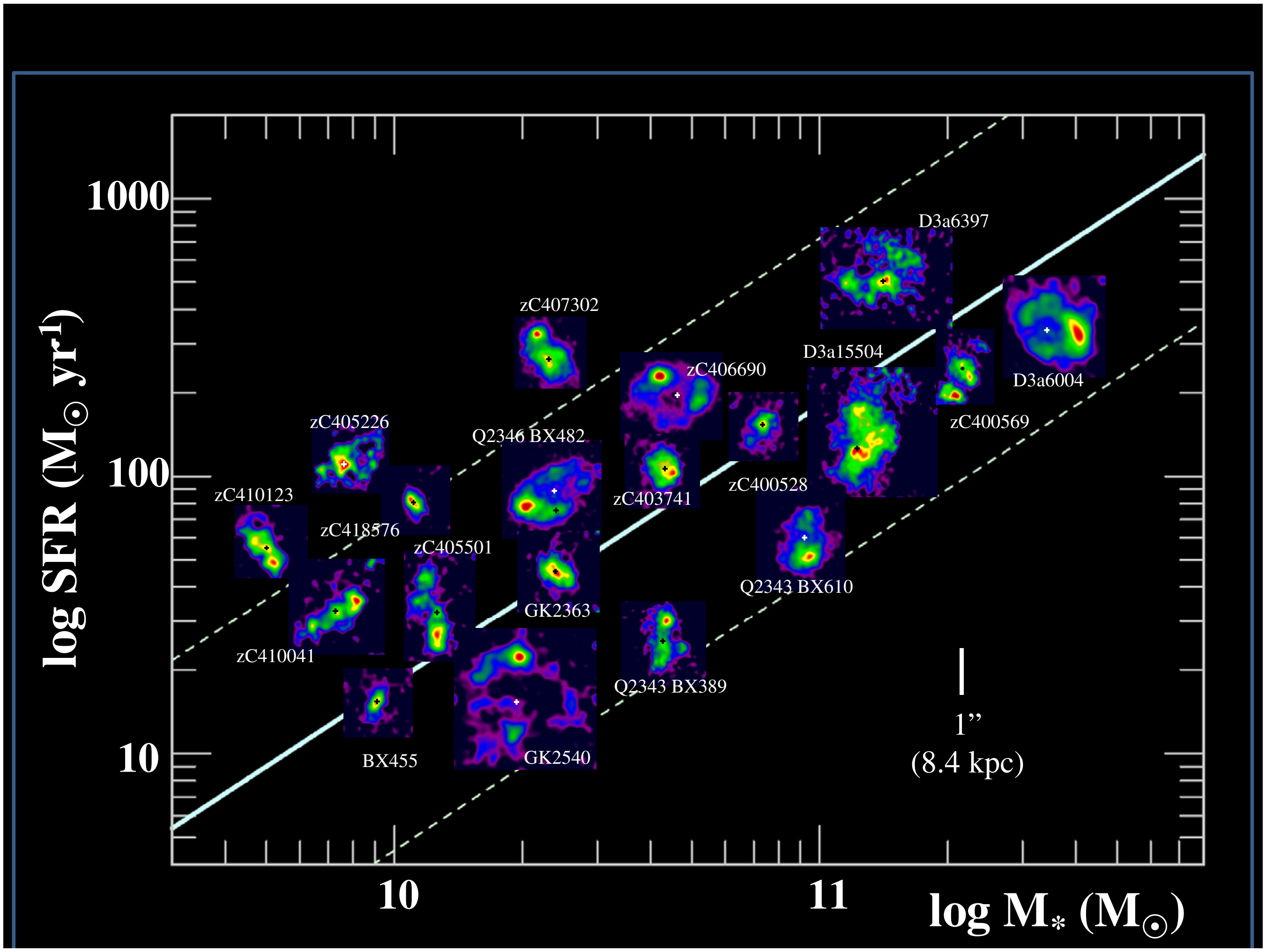

Figure 1. Integrated Hα maps of the 19 disks in this paper, in the stellar mass–SFR plane. The FWHM angular resolution of these maps is $\sim 0\farcs21$–$0\farcs27$, and all galaxies are on the same angular scale (the white vertical bar indicates 1$''$ ($\sim$8.4 kpc)). The color scale of the brightness distributions is linear and auto-scaled. The continuous white line marks the location of the $z \sim 2$ "main sequence" with an assumed slope of 1 (sSFR = SFR/M_* = Const; e.g., Daddi et al. 2007; Rodighiero et al. 2010; Whitaker et al. 2012), with the dashed lines denoting SFRs $\sim$ 4 times above and below the white line, roughly indicating the scatter of the star formation main sequence. Several of the images are rotated in order to better fit onto the plot.

(A color version of this figure is available in the online journal.)

dispersion σ for each pixel, along with their fit errors. The bottom three panels in Figures 2–20 give the results for all our 19 program galaxies. To determine the kinematic center and position angle (p.a.) of the major axis, we first extracted two-dimensional velocity fields and then determined the position at the centroid along the direction of the maximum velocity gradient. The high data quality for all 19 galaxies allows us to determine accurately the kinematic center, as can be seen from the observed kinematic profiles of Figures 2–20. In particular, since the velocity curves clearly display a turnover at large radii, the position of zero-velocity crossing is tightly constrained and coincides with the observed peak in velocity dispersion.

As we are here carrying out a dynamical analysis of rotation-dominated galaxies based on spatially resolved kinematic data, the relevant center is the kinematic center. The Hα light or even the rest-optical continuum emission probed in the near-IR for $z \sim 2$ galaxies can be significantly affected by the contribution from more recent or intense star formation, and by non-uniform dust extinction (e.g., Maraston et al. 2010; Wuyts et al. 2012). These effects could possibly impact the determination of the center based on the emission alone, further justifying our choice of kinematic center as a reliable determination of the true center of our systems. Nevertheless, we measured the offset between the kinematic center and the centroid of the H-/K-band continuum for our sample galaxies and explored whether the derived Hα structural properties (centroid, scale length, and ring size (see below)) change if we would have taken the H-/K-band continuum centroid instead. In all but three cases this centroid is identical within about two pixels ($0\farcs1$) of the center of symmetry of ellipses matched to the outer isophotes of the Hα surface brightness distributions (Figures 21 and 22), or of the peak of the H-/K-band continuum emission. The interpretation of this comparison is somewhat unclear, however, because of the typically clumpy, asymmetric brightness distributions of the UV/optical rest band emission in many, and especially in the smaller, lower mass SFGs (see Wuyts et al. 2012; see also Förster Schreiber et al. 2011a). A more relevant statement can be made if we restrict the comparison to the eight "nucleated" SFGs with a clearly identifiable central bulge,

Table 1
Properties of the Galaxies

Galaxy	sSFR Gyr^{-1}	Re(Hα) (kpc)	del-Re (kpc)	log$M*$ ($M_{\odot}$)	log(M_dyn) ($M_{\odot}$)	del-log$M$ ($M_{\odot}$)	Mass-Model	Hα Distribution	κ_inner (km s^{-1} kpc^{-1})	logΣ_{molgas}inner ($M_{\odot}$ pc^{-2})	log$\Sigma*$inner ($M_{\odot}$ pc^{-2})	Q_inner	del-Q	Q_outer	del-Q
zC415876	7.0	1.8	0.3	9.96	10.36	0.15	Exponential	Exponential	391	3.20	2.40	0.98	0.10	0.49	0.07
BX 455	3.7	2.7	0.5	10.00	10.40	0.10	Exponential	Exponential	400	3.04		1.40	0.09	0.70	0.13
zC403741	1.5	2.5	0.4	10.64	10.50	0.17	Exponential	Ring + Exponential	400	2.65		1.78	0.12	0.85	0.06
GK 2363	3.2	2.5	0.7	9.97	10.52	0.14	Exponential	Exponential	400	3.21		0.54	0.06	0.29	0.04
zC405226	8.4	4.4	0.7	9.97	10.58	0.11	Exponential	Exponential	190	2.85	2.54	1.29	0.26	0.43	0.14
zC405501	11.1	7.7	1.3	9.92	10.68	0.11	Ring + Bulge	Ring + Bulge	125	2.56	2.53	1.29	0.14	0.18	0.01
zC410041	11.3	5.5	0.9	9.66	10.73	0.18	Exponential	Exponential + Ring	220	2.72		1.57	0.35	0.30	0.06
zC410123	12.6	4.8	0.8	9.62	10.78	0.18	Exponential	Exponential + Ring	230	2.73	2.71	1.85	0.28	0.60	0.08
zC400528	1.4	1.6	0.3	11.00	10.85	0.21	Exponential	Exponential (+ Ring?)	650	3.45	3.37	0.75	0.05	0.38	0.08
GK 2540	0.8	11.2	1.9	10.28	10.93	0.25	Exponential	Ring + Exponential	230	1.27		5.27	3.00	1.58	0.39
zC407302	12.3	4.6	0.8	10.38	11.04	0.25	Exponential	Exponential	460	3.43	2.73	0.85	0.03	0.38	0.08
D3a6397	3.8	6.2	1.1	11.08	11.15	0.21	Bulge + Ring	Ring + Bulge	550	3.17		0.91	0.10	0.18	0.02
BX 482	4.9	5.5	0.9	10.30	11.20	0.24	Exponential	Ring (+Expon.)	500	2.27	2.41	6.82	1.07	0.61	0.13
zC400569	1.4	5.7	1.0	11.08	11.26	0.10	Exponential + Bulge	Exponential (+ Compact ring ?)	900	3.39	4.05	1.25	0.21	0.37	0.08
D3a15504	1.5	6.7	1.1	10.89	11.28	0.10	Exponential + Bulge	Exponential	700	2.94	3.49	2.35	0.16	0.52	0.04
zC406690	5.3	5.5	0.9	10.60	11.34	0.14	Exponential	Ring (+Expon.)	1062	2.41	2.23	12.13	3.00	0.83	0.09
D3a6004	1.4	5.6	1.0	11.48	11.36	0.16	Bulge +Ring	Ring + Bulge	1000	2.68	4.06	5.16	0.96	0.51	0.07
BX 610	0.8	4.9	0.8	11.00	11.38	0.14	Exponential + Bulge	Ring + Exponential	450	2.62	3.26	5.27	0.62	0.70	0.08
BX 389	2.7	6.8	1.2	10.60	11.41	0.18	Ring	Ring	103	2.84	2.45	0.99	0.09	0.81	0.07

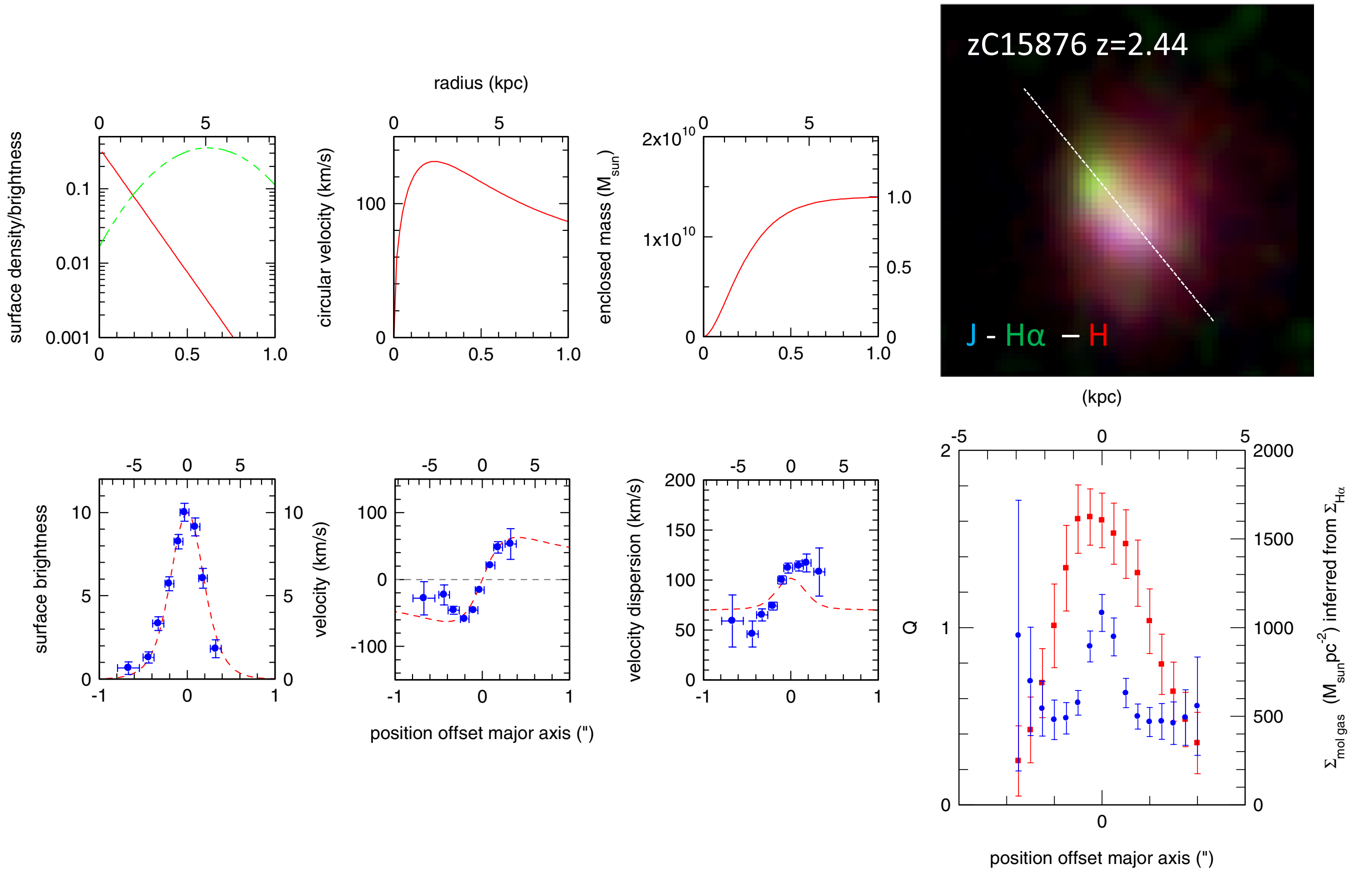

Figure 2. Results of the dynamical modeling of the individual galaxies. The three bottom panels show the observed Hα surface brightness (left, normalized to 0–10), velocity (middle), and velocity dispersion (right) distributions as blue filled circles, as a function of major-axis offset (along the dotted white line in the upper right Hα, or Hα+continuum images). The typical software slit width perpendicular to the major axis is 0.″25–0.″3. As described in Section 2.2, we created simple rotating disks with one or two mass and Hα luminosity density components to fit these data. The surface density, circular velocity, and dynamical mass distributions of these input models are shown as red continuous lines in the top row; in some of the cases the surface brightness models (dotted red lines in the upper left) differ from the mass distributions. The projection of these models onto the major-axis software slits, smoothed to the spatial and spectral instrumental resolutions, is shown as red dotted curves in the lower three panels. The bottom right panel compares the distributions of the inferred molecular surface density distribution (red, right axis) and of the inferred Toomre Q-parameter (filled blue circles, left axis) along the kinematic major axis. The molecular gas masses and column densities (including a 36% correction for He) are inferred from the observed (narrow component) Hα surface brightness distributions, corrected for global extinction with a "double"-Calzetti recipe, then converted to SFR surface density with the standard conversion factor of Kennicutt (1998a, 1998b, but for a Chabrier IMF), and finally converted to molecular column density with the Tacconi et al. (2013) calibration from PHIBSS, as described in Section 2.2 (point (4)). The *HST* WFC3 J/H images used in the upper right panels are from S. Tacchella et al. (in preparation); in a few cases we also used the continuum from the SINFONI cubes themselves. A blue arrow in the bottom panels indicates the location of the H-/K-band continuum center relative to the kinematic center (which defines the reference zero offset along the major axis) for the following galaxies: zC400528, zC407302, D3a6397, Q2346-BX 482, zC400569, D3a15504, D3a6004, and Q2343-BX 610 (see Section 2.2). The figures are sorted from low to high dynamical mass, as in Table 1.

(A color version of this figure is available in the online journal.)

on either our SINFONI continuum maps or the WFC3 H-band *HST* maps of S. Tacchella et al. (in preparation). In these cases we find that the average separation between the kinematic centroid and the nuclear continuum peak is 0.″1 (±0.″1), and in no case larger than a resolution element (∼0.″2). Only in one case is the inferred separation significant at more than twice the measurement uncertainty (D3a 15504). This centering uncertainty is typically equivalent to 20% of the Hα half-light radius (or ring radius). Given that the widths of the Hα rings discussed below are about half of this radius, the centering methodology thus does not have a significant impact on the deduced Hα structural properties.

The impact on the kinematic profiles of Figures 2–20 is also not significant. Indeed, the typical offsets between the kinematic and continuum centers are smaller than the 0.″25–0.″3 width of the slit (i.e. 5–6 pixels) along which we extracted the major-axis profiles for the dynamical analysis. Moreover, these offsets are mostly along the minor axis of the galaxies such that the effective difference in the location of the kinematic and continuum center along the major-axis profiles is typically even less than 0.″1. This is illustrated in the subset of Figures 2–20 for the eight "nucleated" galaxies, i.e., for which the continuum center can most confidently be interpreted as tracing the centroid of distribution of the bulk of the stellar component, where we plot arrows corresponding to the location of the continuum center along the major-axis profiles.

2. *Disk modeling*. We constructed rotating disk models, fitting the observational constraints $I(p)$, $v(p)$, and $\sigma(p)$ as a function of projected major-axis position offset p, from the kinematic/stellar centroid of the galaxy. These disk models compute data cubes from input structural parameters (see Cresci et al. 2009). The main parameters are the disk's center position, its inclination and major-axis orientation on the sky, as well as its mass and light distributions as a

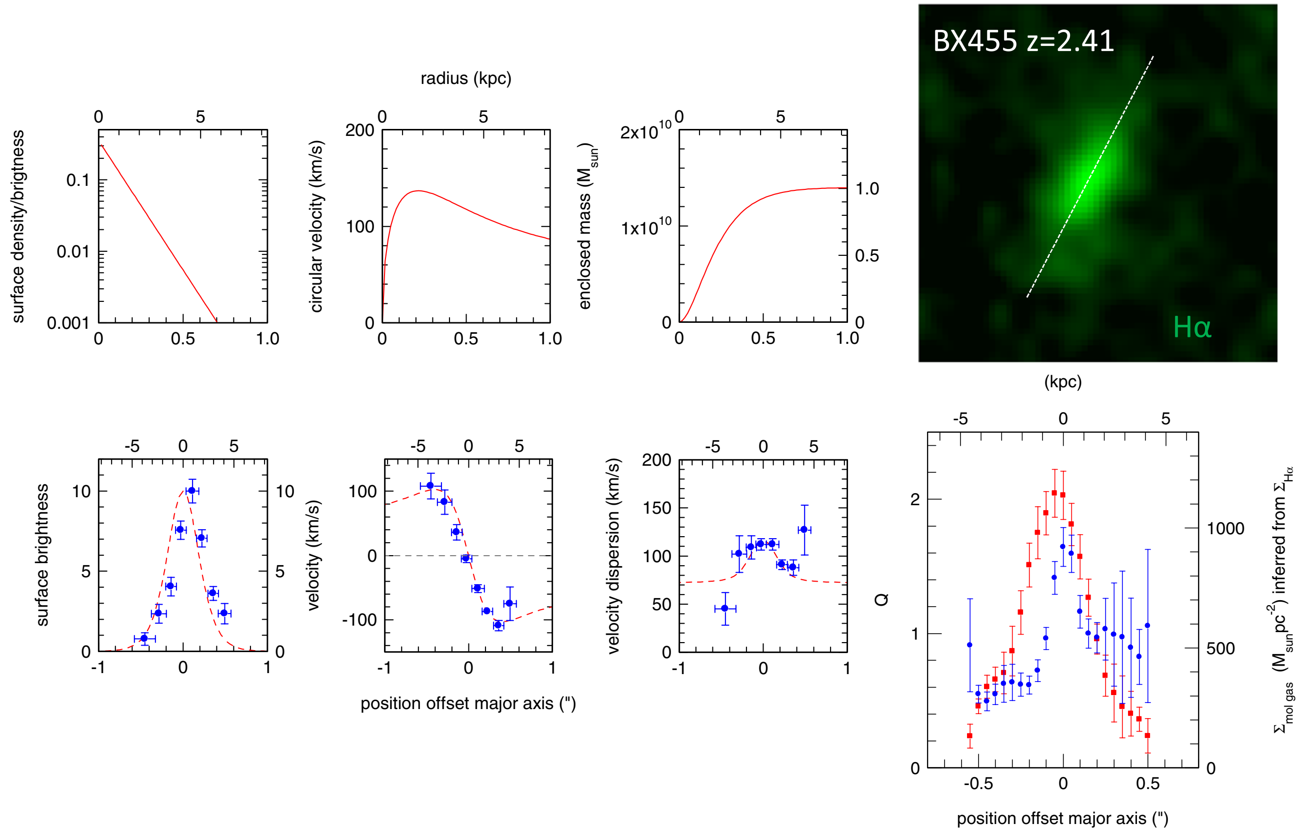

Figure 3. Same as Figure 2.
(A color version of this figure is available in the online journal.)

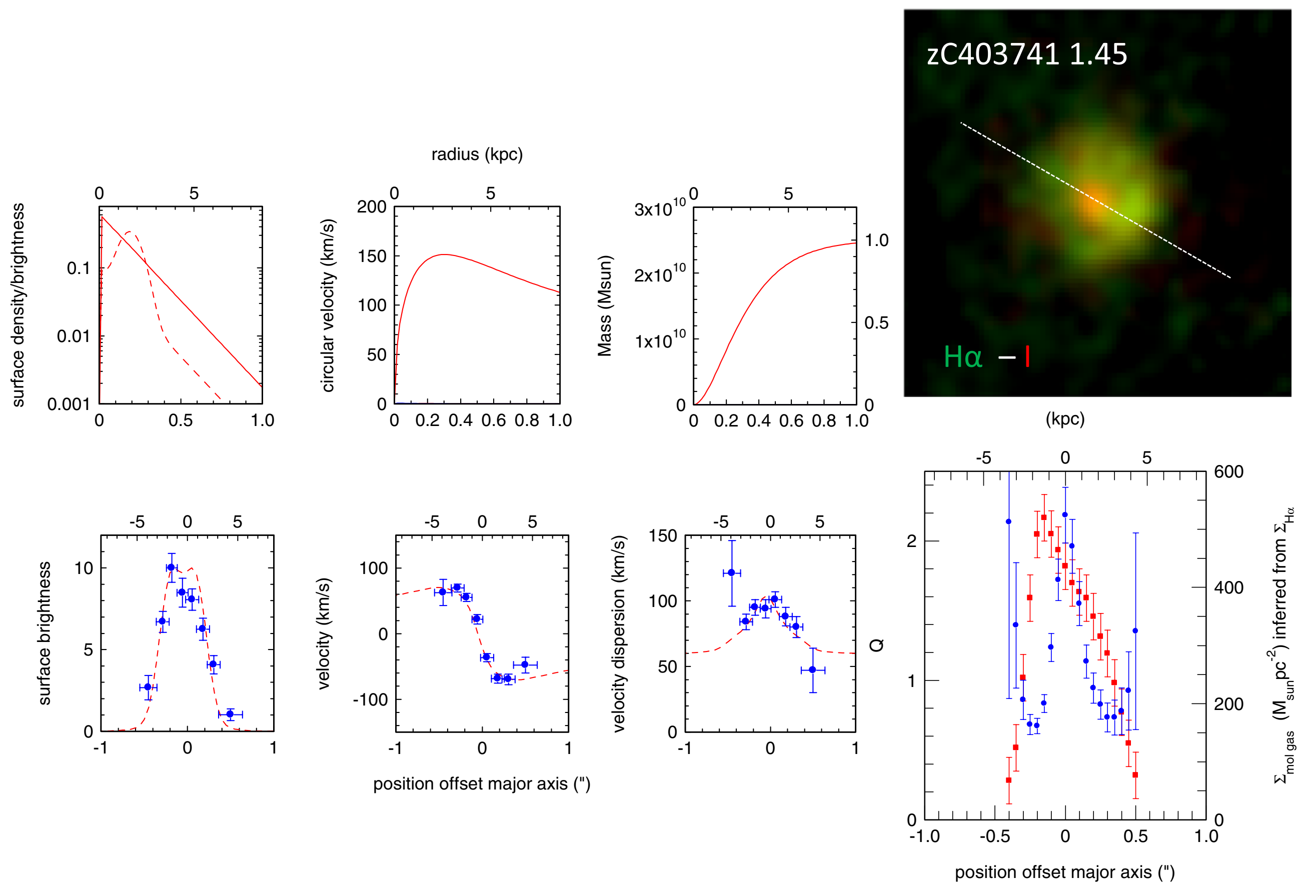

Figure 4. Same as Figure 2.
(A color version of this figure is available in the online journal.)

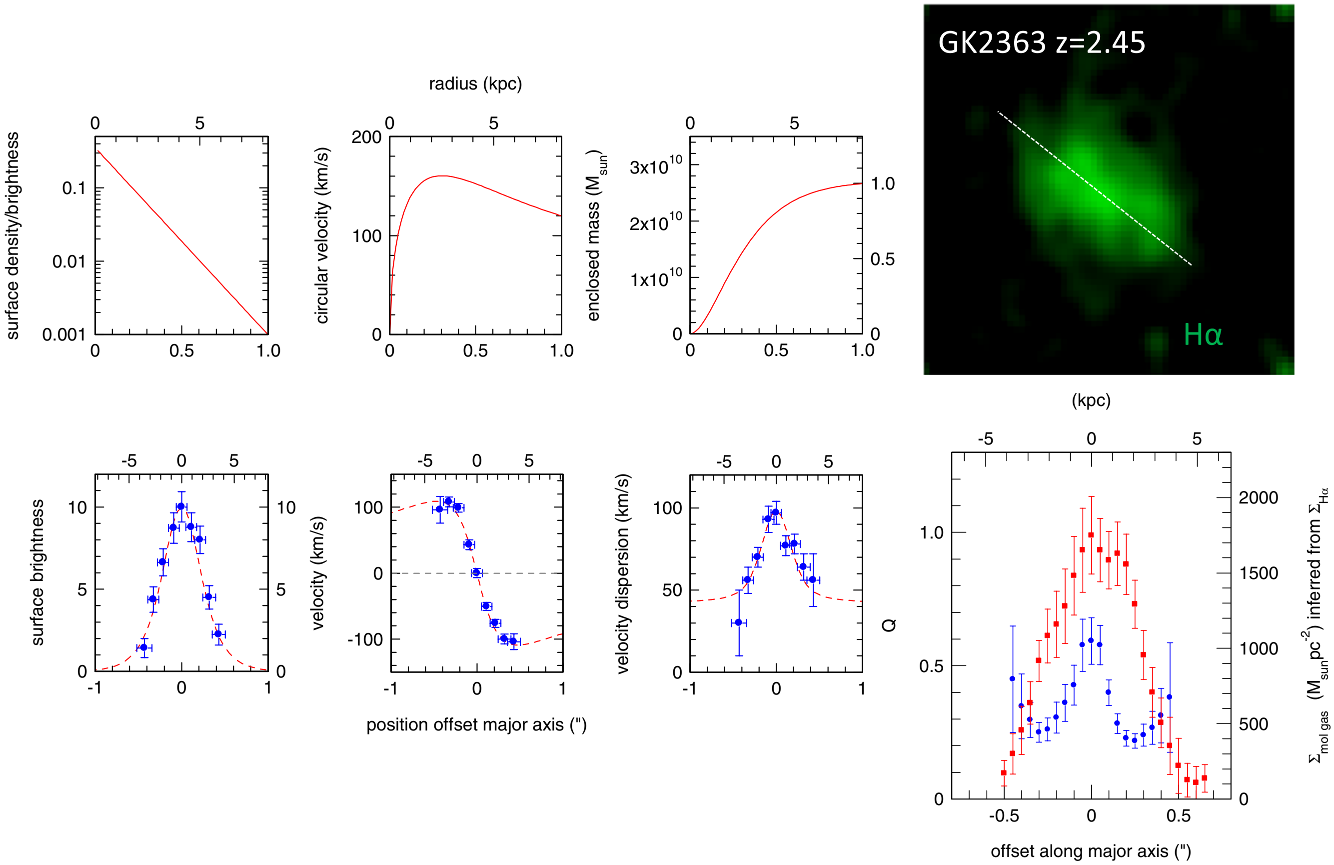

Figure 5. Same as Figure 2.

(A color version of this figure is available in the online journal.)

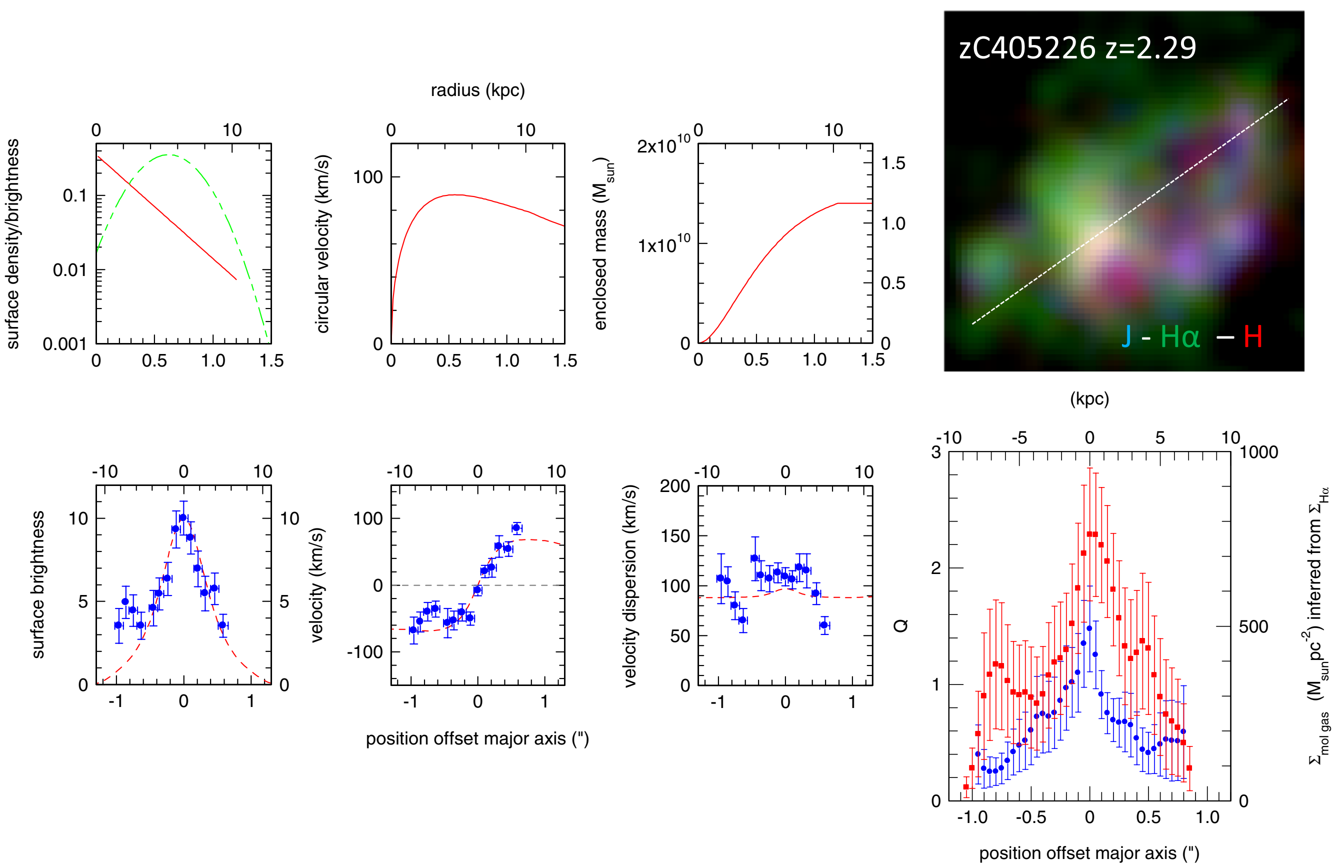

Figure 6. Same as Figure 2.

(A color version of this figure is available in the online journal.)

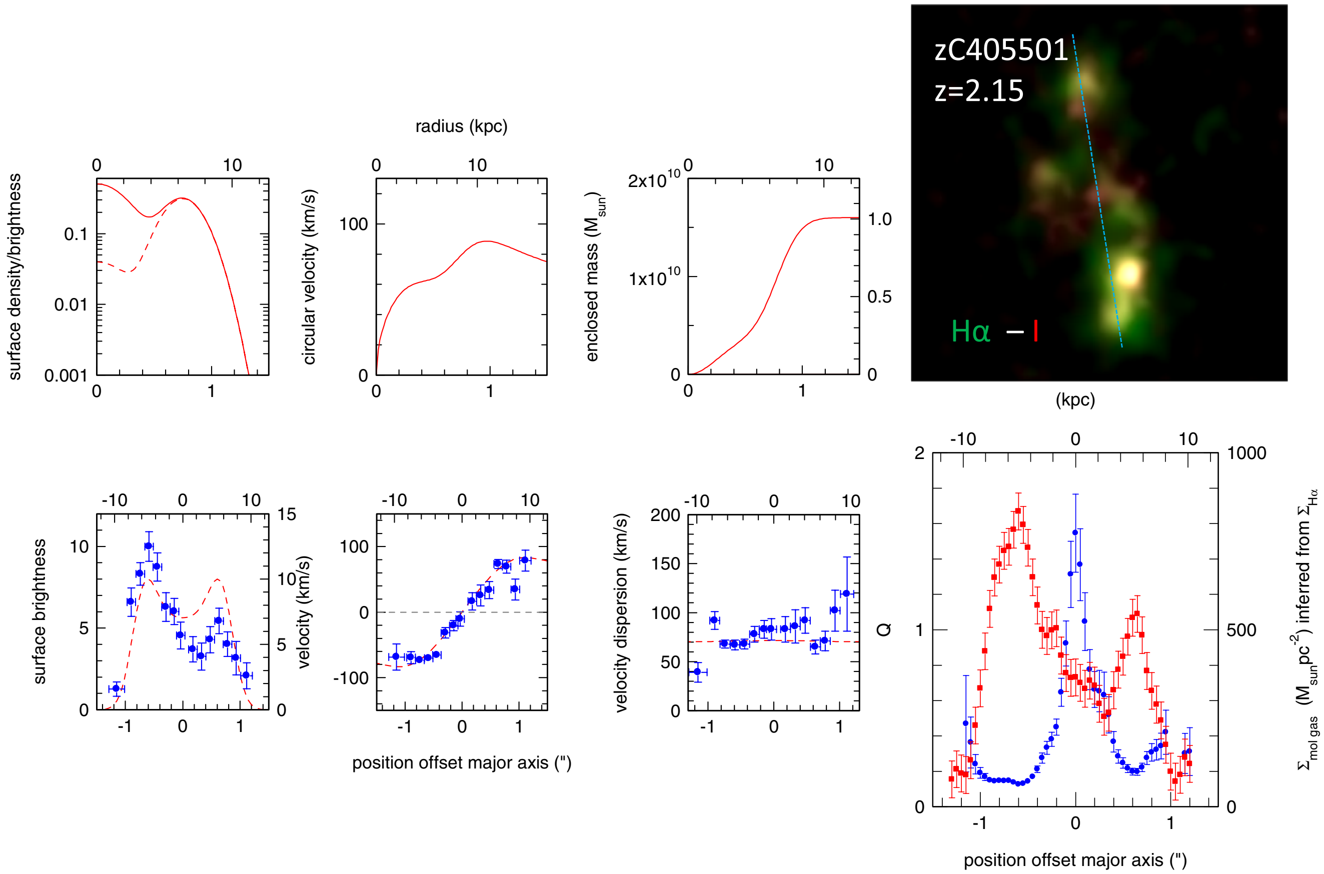

Figure 7. Same as Figure 2.

(A color version of this figure is available in the online journal.)

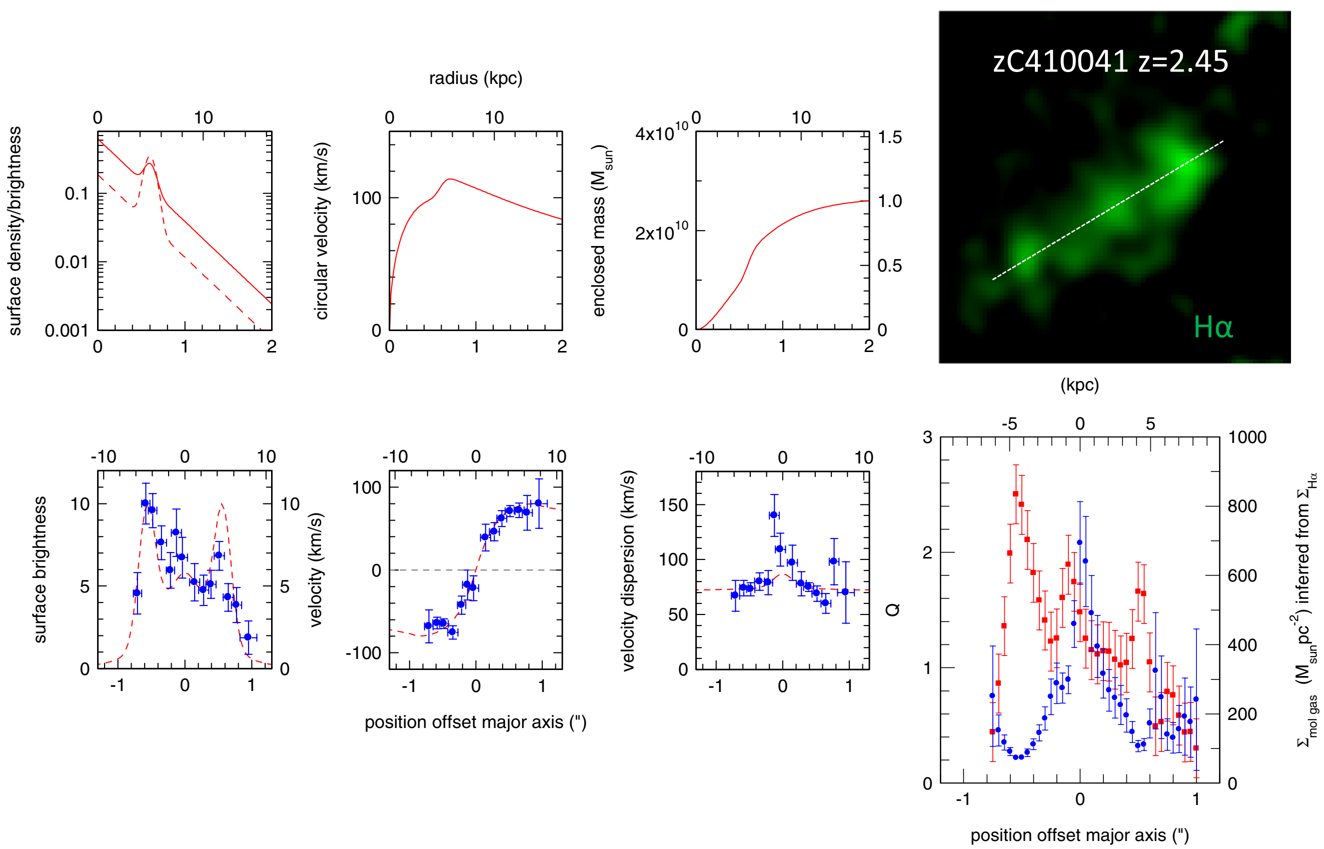

Figure 8. Same as Figure 2.

(A color version of this figure is available in the online journal.)

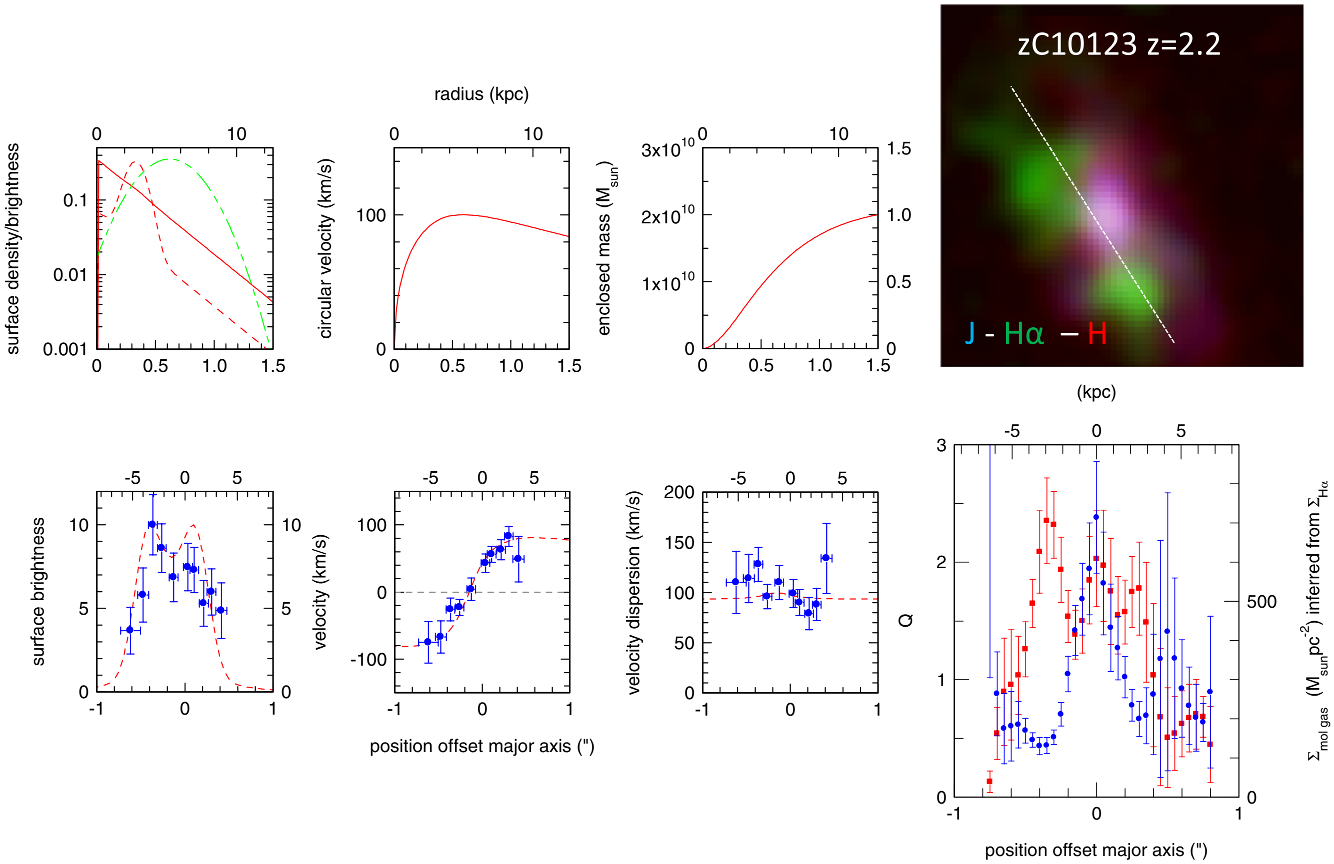

Figure 9. Same as Figure 2.

(A color version of this figure is available in the online journal.)

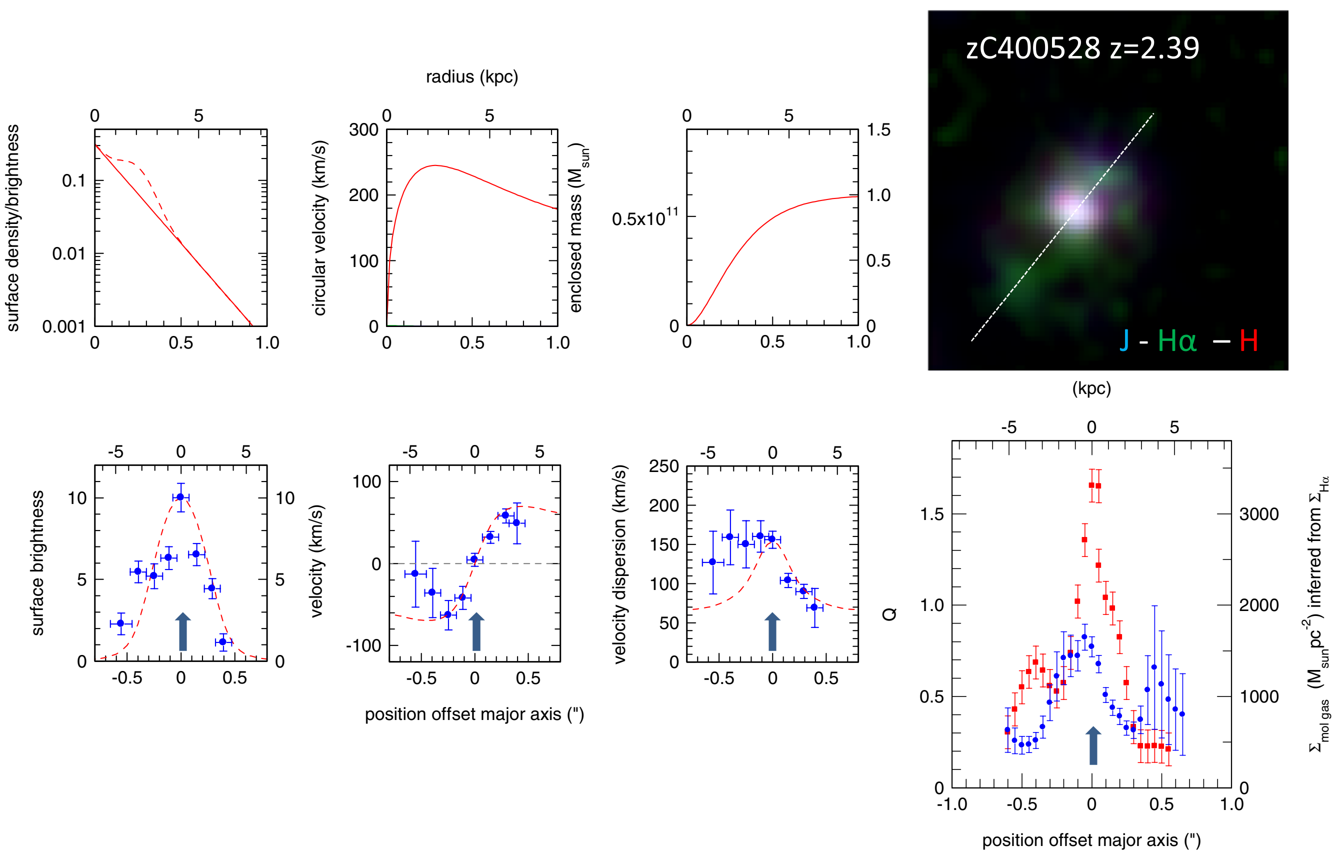

Figure 10. Same as Figure 2.

(A color version of this figure is available in the online journal.)

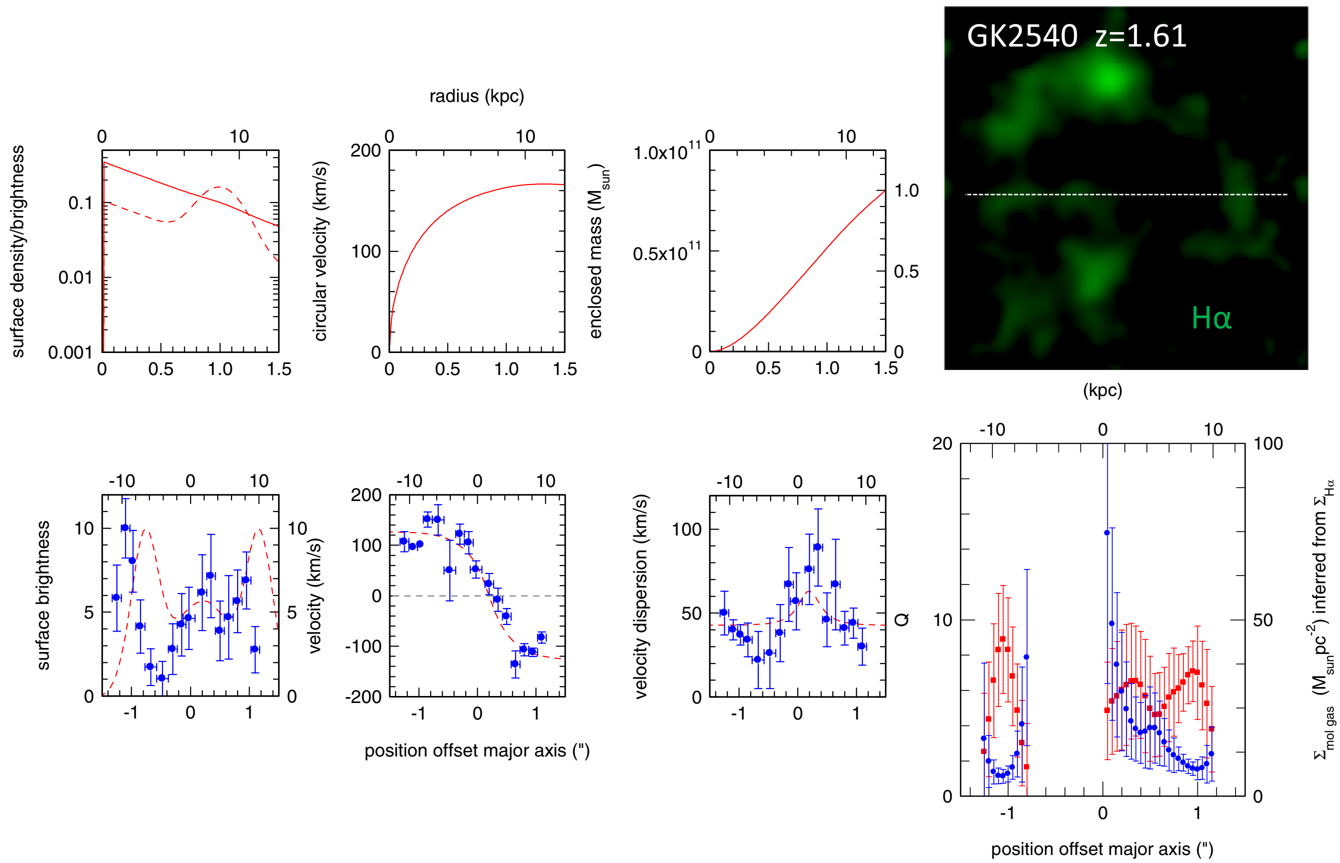

Figure 11. Same as Figure 2.

(A color version of this figure is available in the online journal.)

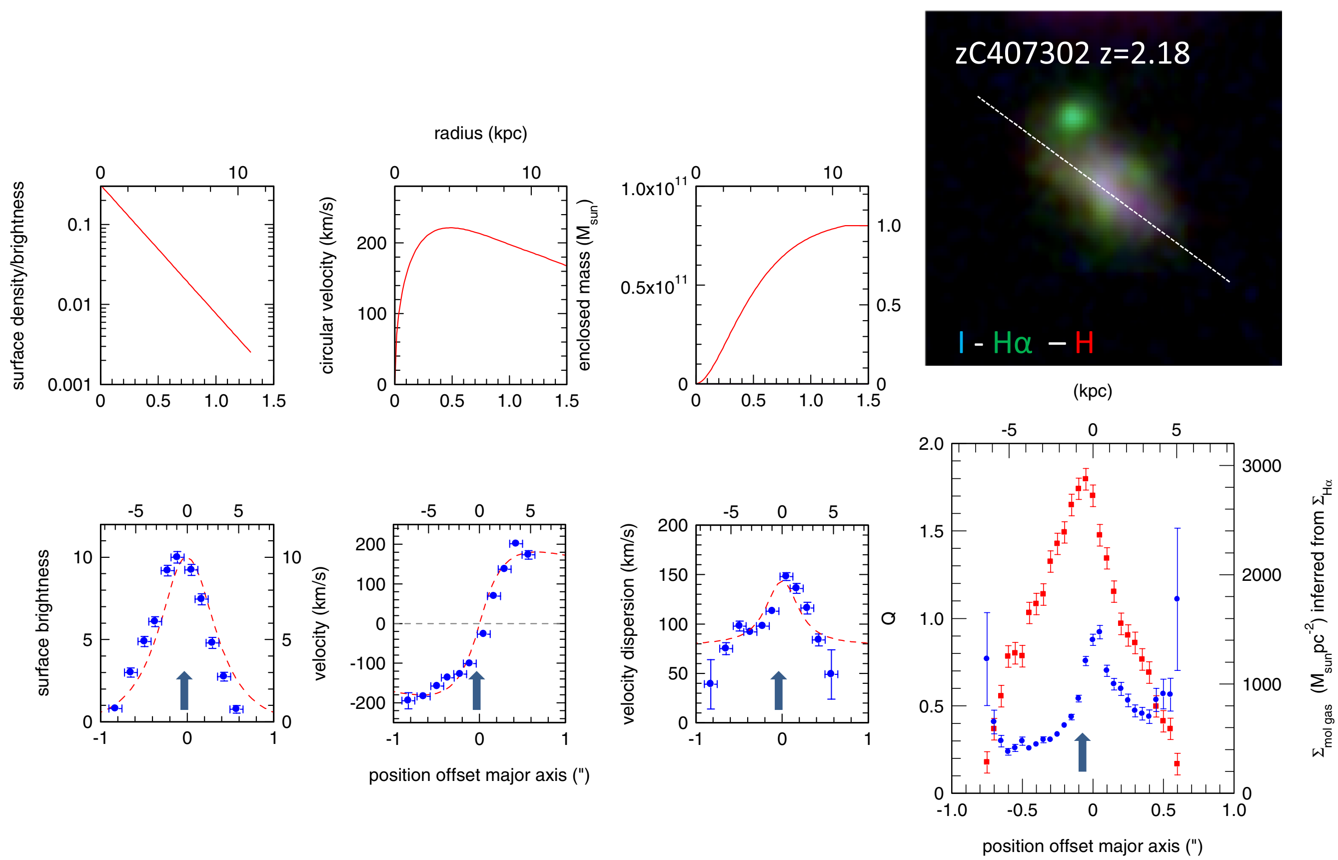

Figure 12. Same as Figure 2.

(A color version of this figure is available in the online journal.)

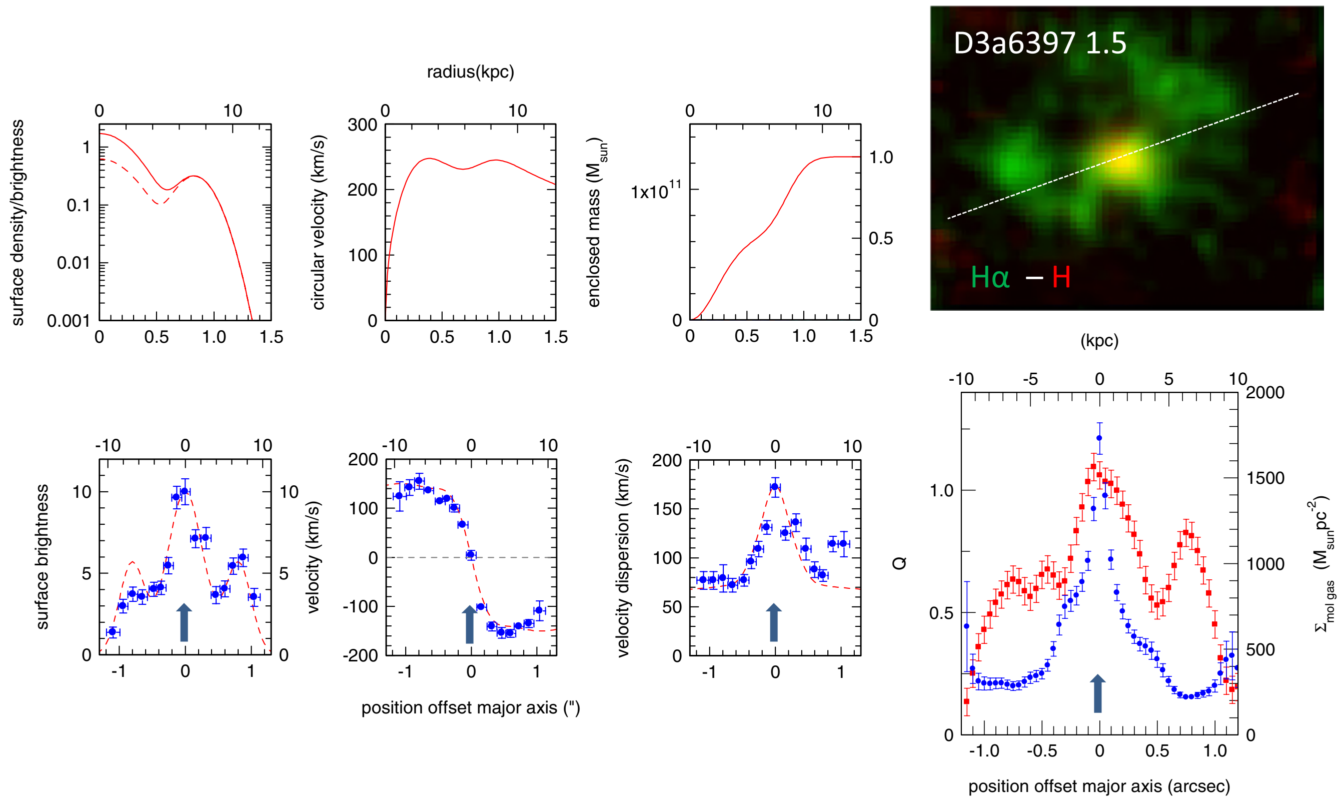

Figure 13. Same as Figure 2.

(A color version of this figure is available in the online journal.)

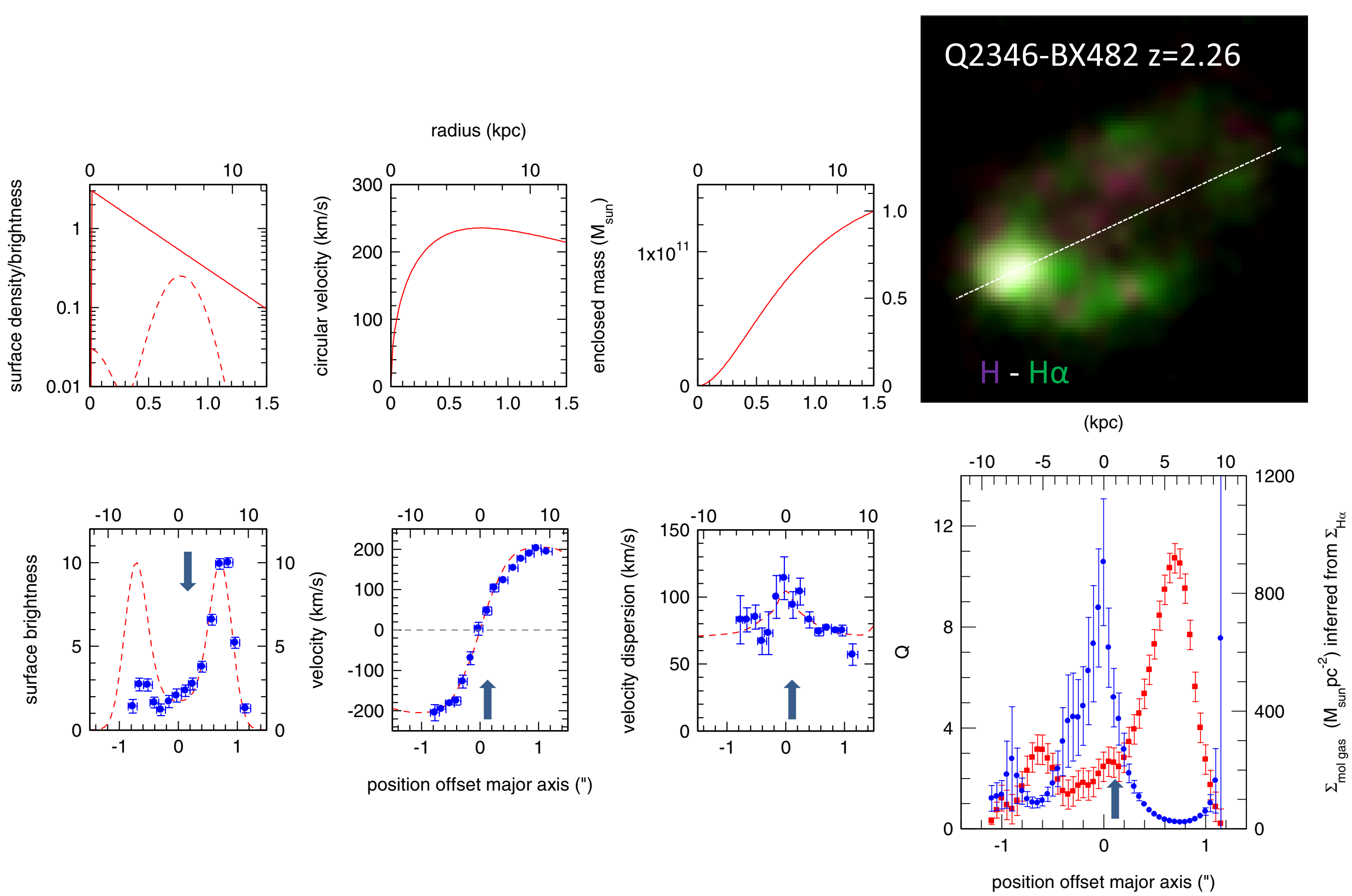

Figure 14. Same as Figure 2.

(A color version of this figure is available in the online journal.)

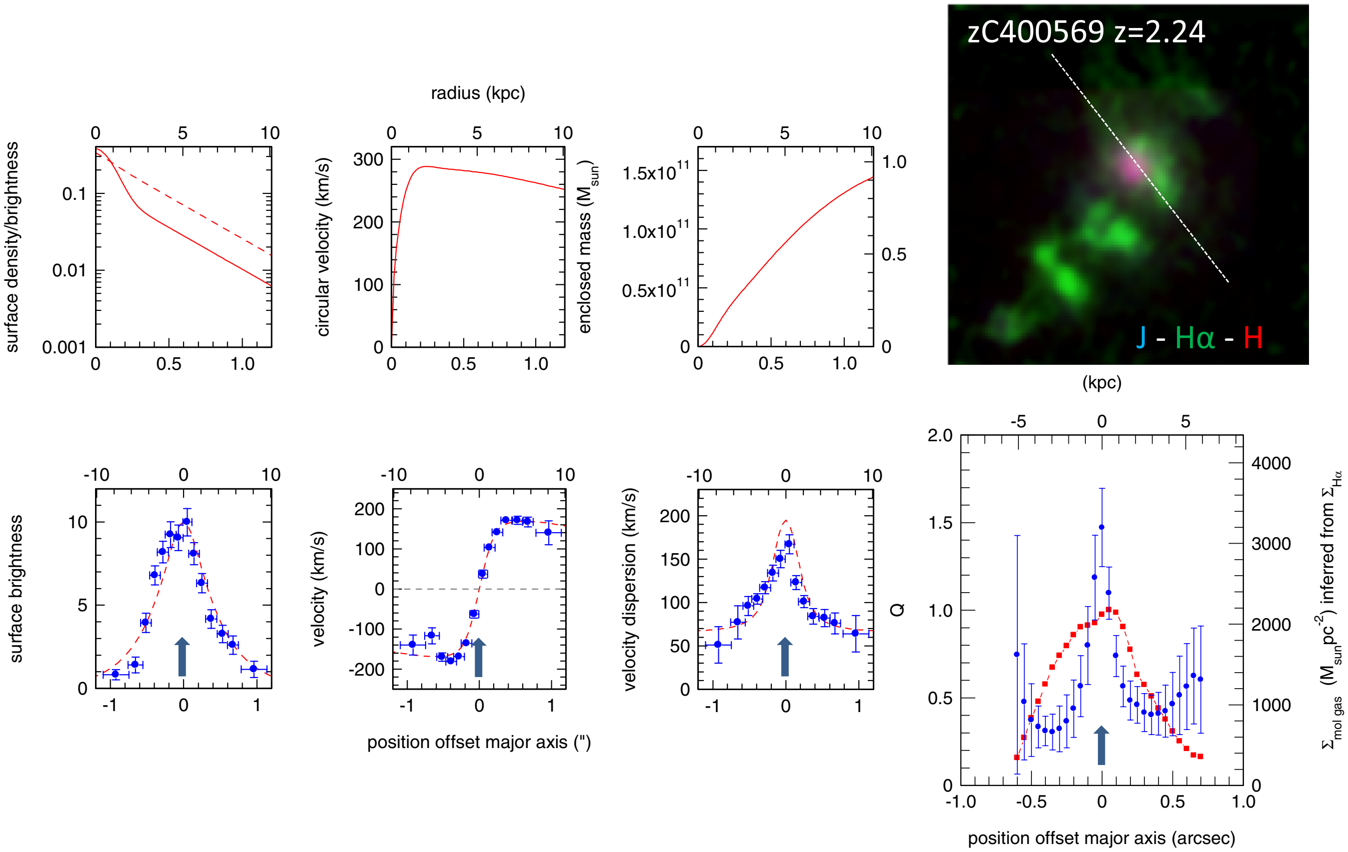

Figure 15. Same as Figure 2.

(A color version of this figure is available in the online journal.)

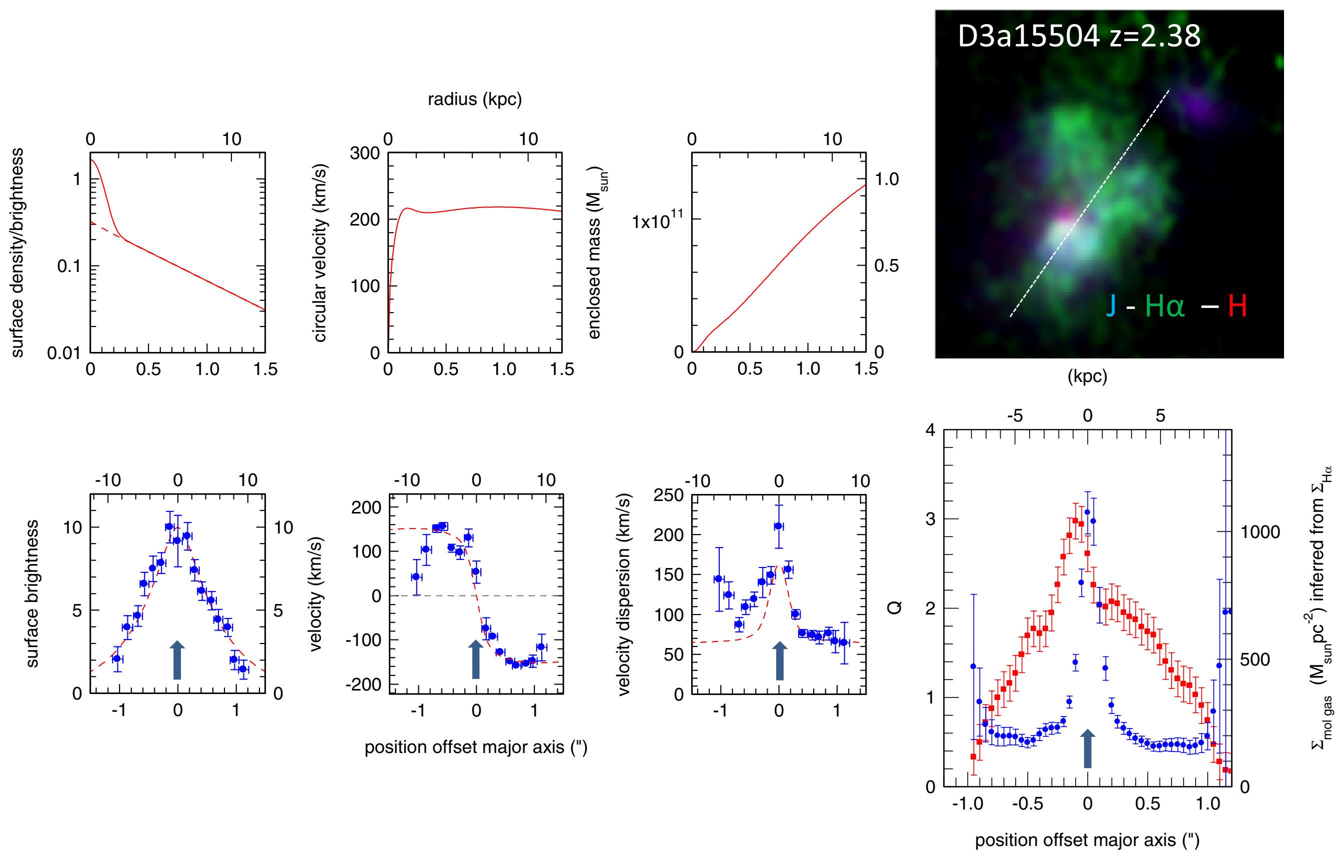

Figure 16. Same as Figure 2.

(A color version of this figure is available in the online journal.)

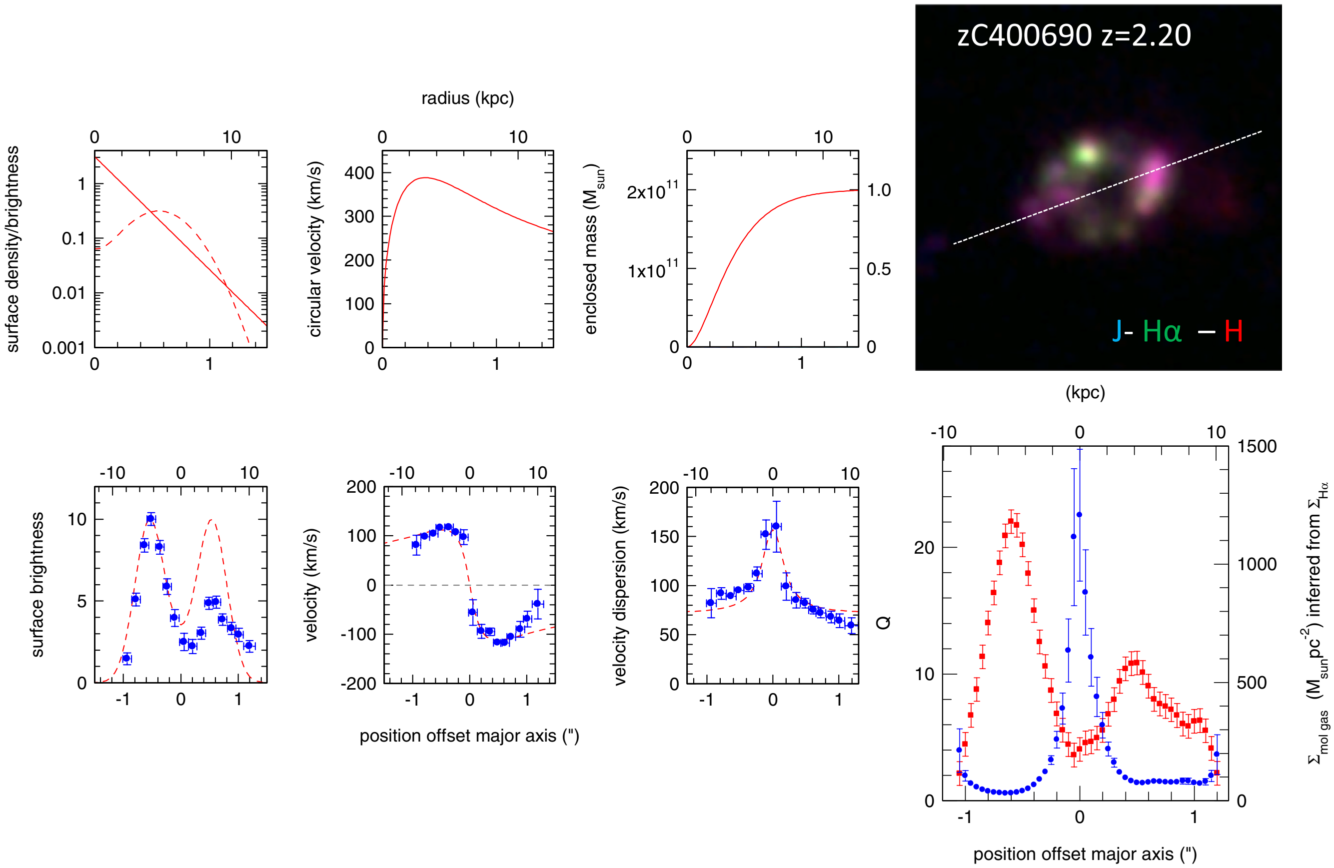

Figure 17. Same as Figure 2.
(A color version of this figure is available in the online journal.)

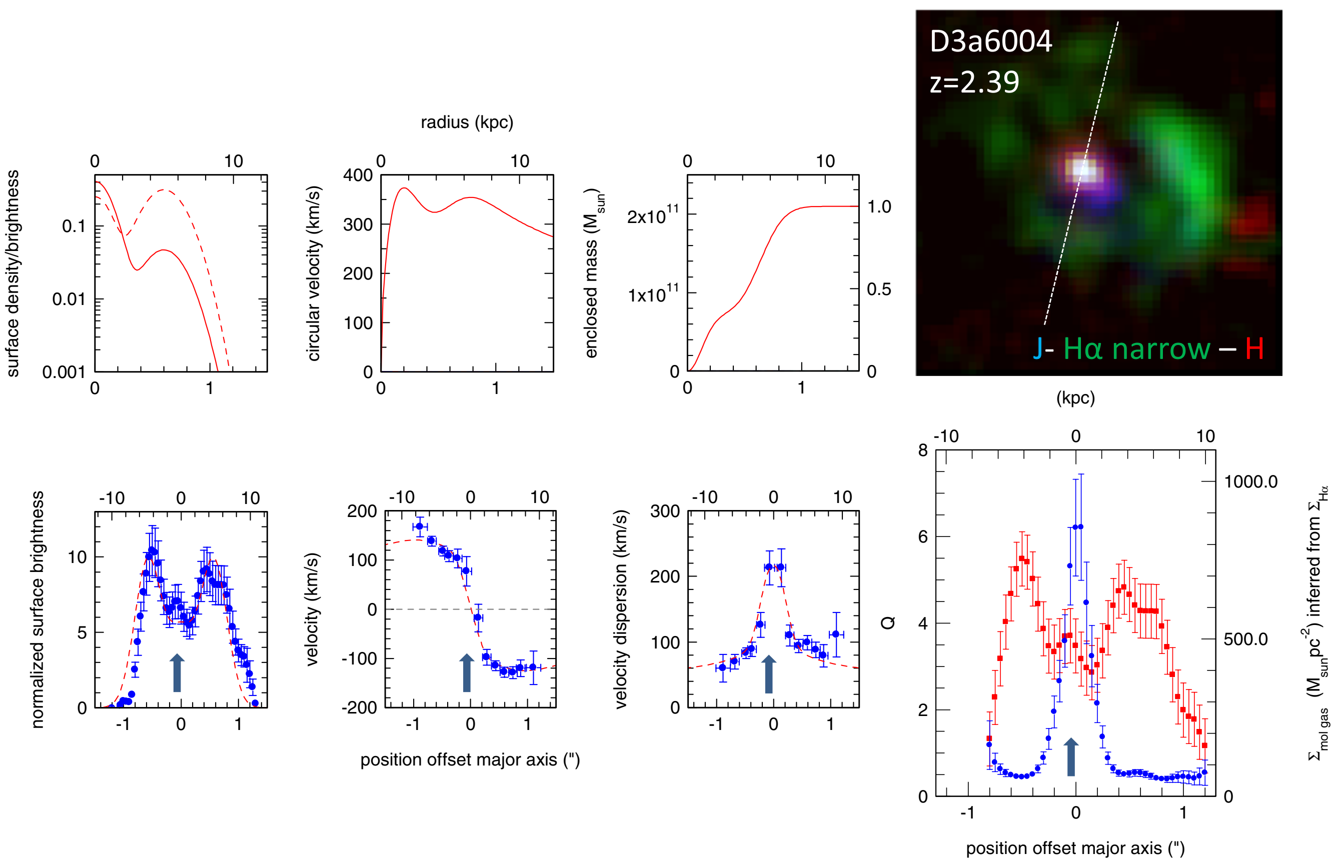

Figure 18. Same as Figure 2.
(A color version of this figure is available in the online journal.)

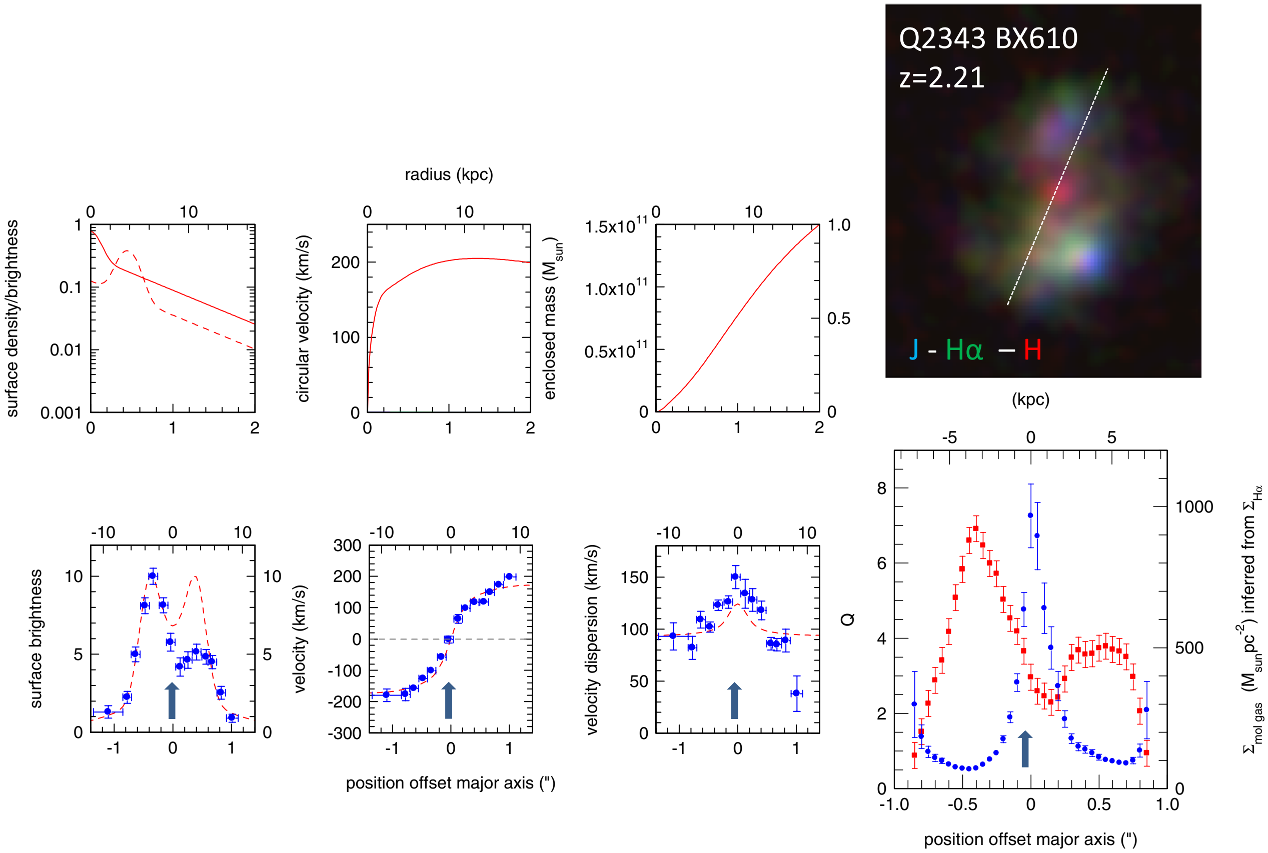

Figure 19. Same as Figure 2.
(A color version of this figure is available in the online journal.)

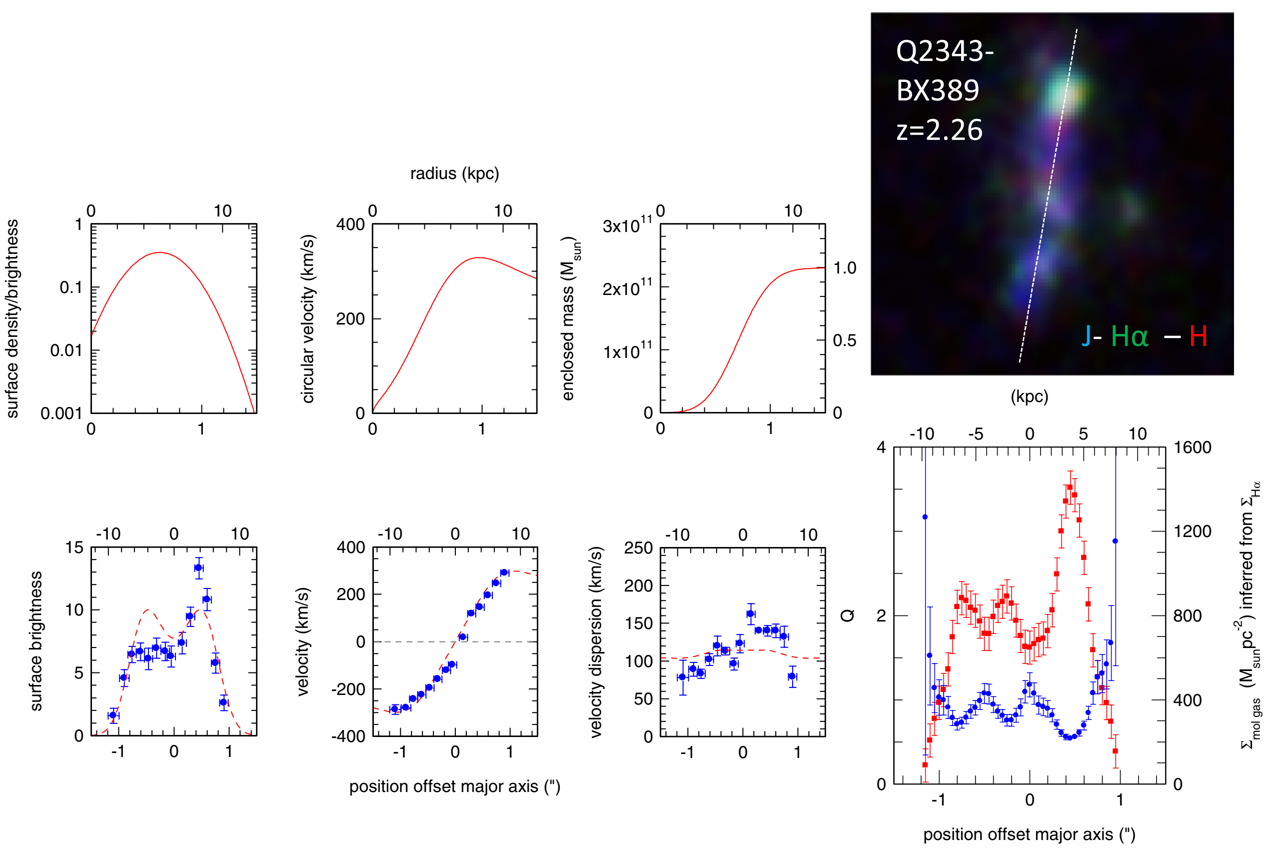

Figure 20. Same as Figure 2.
(A color version of this figure is available in the online journal.)

function of radius, its total dynamical mass, and a constant additional velocity dispersion assumed to be isotropic. Position angle, inclination, and centroid are determined from the morphology of the Hα and (where possible) *HST* images, and (for the centroid) from the zero crossing of the observed rotation curve, assuming reflection symmetry in velocity along the major axis. The model data are then convolved with the angular and spectral resolution instrumental profiles and sampled at the observed pixel scale. Surface brightness, velocity, and velocity dispersion cuts along the major axis are then extracted as for the data. The total dynamical mass M_{dyn} and the light and mass distributions (not necessarily identical) are then varied to achieve a fit to the data along the major axis. We have also carried out two-dimensional (2D) fitting of I, v, and σ but find that the major-axis information captures the essential information needed for the modeling.

In all cases we start with the assumption of an exponential distribution in both mass and Hα light, with a half-mass/light radius taken from the analysis in FS14, based on 2D Sérsic fitting and a curve-of-growth analysis of the integrated Hα flux distribution. In 11–13 SFGs of the sample an exponential is not a good fit to the Hα light distribution (Table 1, Figures 2–22). A Gaussian ring, or a ring plus an exponential, is then adopted to better match the major-axis surface brightness profiles. The average Hα ring radius in Table 1 is 4.5 kpc, but there is a large scatter from 1.5 to 9 kpc. The ring structures are not an artifact of off-center clumps along the major axis. This is shown in Figures 21 and 22, where we present radial profiles based on the Hα surface brightness distributions from Figure 1, averaged in elliptical annuli with center and p.a. corresponding to the kinematic center and major axis, with axis ratio matched to the outer narrow Hα isophotes, and with width of $0\farcs1$ (along the major axis). These profiles compare well with the major-axis cuts shown in Figures 2–20 and adopted in our analysis. All cases for which we find Hα peaks off-center in the major-axis distribution (see below) also exhibit a ring structure in their radial profiles. Varying the adopted center position by 1–2 pixels in each spatial direction shows that the excess flux outside of the nuclear regions indicative of a ring is a qualitatively robust feature of the galaxies, although the exact details of the profiles (in particular the amplitude and radius of the ring feature) depend somewhat on the adopted center. We note again that the data quality and the observed turnover of the velocity curves and peak of the velocity dispersion profiles allow a very accurate determination of the kinematic center. Forcing the center position at the continuum center instead results in asymmetric kinematic profiles and yields poorer fits to the data. We nonetheless verified for the eight "nucleated" galaxies that, given the properties of the best-fit kinematic model (by construction referred to the kinematic center as defined in point (1) above), the conclusions of our dynamical analysis presented in Section 3 below (in particular the Toomre-Q profiles) are not significantly changed when offsetting the reference position to the continuum center.

3. *Inferred kinematic properties.* In 5 of the 19 cases, the steepness of the central major-axis velocity gradient, combined with a prominent peak of velocity dispersion near the kinematic centroid, requires a mass distribution more compact than an exponential, for instance, the combination of the original $R_{1/2}$ exponential with an additional nuclear mass concentration, assumed for simplicity to be a Gaussian. The specific derived model components and parameters are not unique. However, the velocity data *do* robustly constrain the mass concentration and the rotation curve and give an estimate of its amplitude within the central few kpc, relative to the overall disk. The primary outputs of this modeling are, first, the total dynamical mass within $R \leqslant$ 10–12 kpc (the outer radius of the Hα data); second, the intrinsic velocity dispersion (assumed to be constant and isotropic) required to match the observed velocity dispersion in the outer part of the disk (which is little or not affected by beam-smeared rotation); and third, the intrinsic rotation curve, and thus the epicyclic frequency distribution $\kappa(R)$, as introduced in Section 1. The absolute values of the rotation velocity and dynamical mass depend linearly and in squares on the sine of the inclination, i. The inferred inclinations from the morphological aspect ratio of the Hα and or stellar distribution typically are uncertain to $\pm 5^{\circ}$ up to 20° (e.g., Cresci et al. 2009). This implies uncertainties in velocity and mass of 20%–50% for inclinations $>50^{\circ}$, but can lead in extreme cases to uncertainties of a factor of several for nearly face-on systems. The inclination dependence also affects the overall value of the epicyclic frequency needed to determine Q, but not its radial distribution. The model mass and light, radial surface density distributions, intrinsic rotation curves, and mass distributions are plotted for each of the 19 galaxies in the top three panels of Figures 2–20. In the bottom three panels we compare the projected models, smoothed to the resolution of our observations, with the observed data points.

4. *Inferred molecular gas surface density distribution*. We used the Kennicutt–Schmidt (KS) relation to infer molecular gas surface densities from star formation surface densities. To calculate SFRs from integrated Hα data we applied the conversion of Kennicutt (1998a, 1998b) modified for a Chabrier (2003) IMF (SFR $= L(\mathrm{H}\alpha)_0/2.1 \times 10^{41}$ erg s^{-1}). We first corrected the observed Hα maps for broad emission that originates in outflows (Newman et al. 2012; Förster Schreiber et al. 2013). For this purpose we removed the large-scale velocity shifts due to rotation pixel by pixel, and then computed an integrated "narrow" line Hα map by rejecting Hα emission outside the narrow line core. This method does not, however, correct for the contribution of the broad emission within the narrow line core, which can be substantial in very bright clumps and in nuclear regions (Genzel et al. 2011; Förster Schreiber et al. 2013). In those cases we attempted a more complete removal of the broad emission by two-component fitting in each pixel. We then converted the integrated narrow line Hα map to a star formation surface density map from the Kennicutt (1998b) calibration above. We next corrected the observed star formation surface density map for spatially uniform extinction with a Calzetti (2001) extinction curve ($A(\mathrm{H}\alpha) = 7.4\,E(B-V)$), including the extra "nebular" correction ($A_{\mathrm{gas}} = A_{\mathrm{stars}}/0.44$) introduced by Calzetti (2001). We determined $E\,(B-V)$ from the integrated UV/optical photometry of the galaxies. Förster Schreiber et al. (2009), Mancini et al. (2011), and Wuyts et al. (2011b) find that including the extra nebular correction brings Hα- and UV-continuum-based SFRs of $z \sim 2$ SINS/zC-SINF galaxies into better agreement than without such a correction (but see Reddy et al. 2010; Kashino et al. 2013). However, the

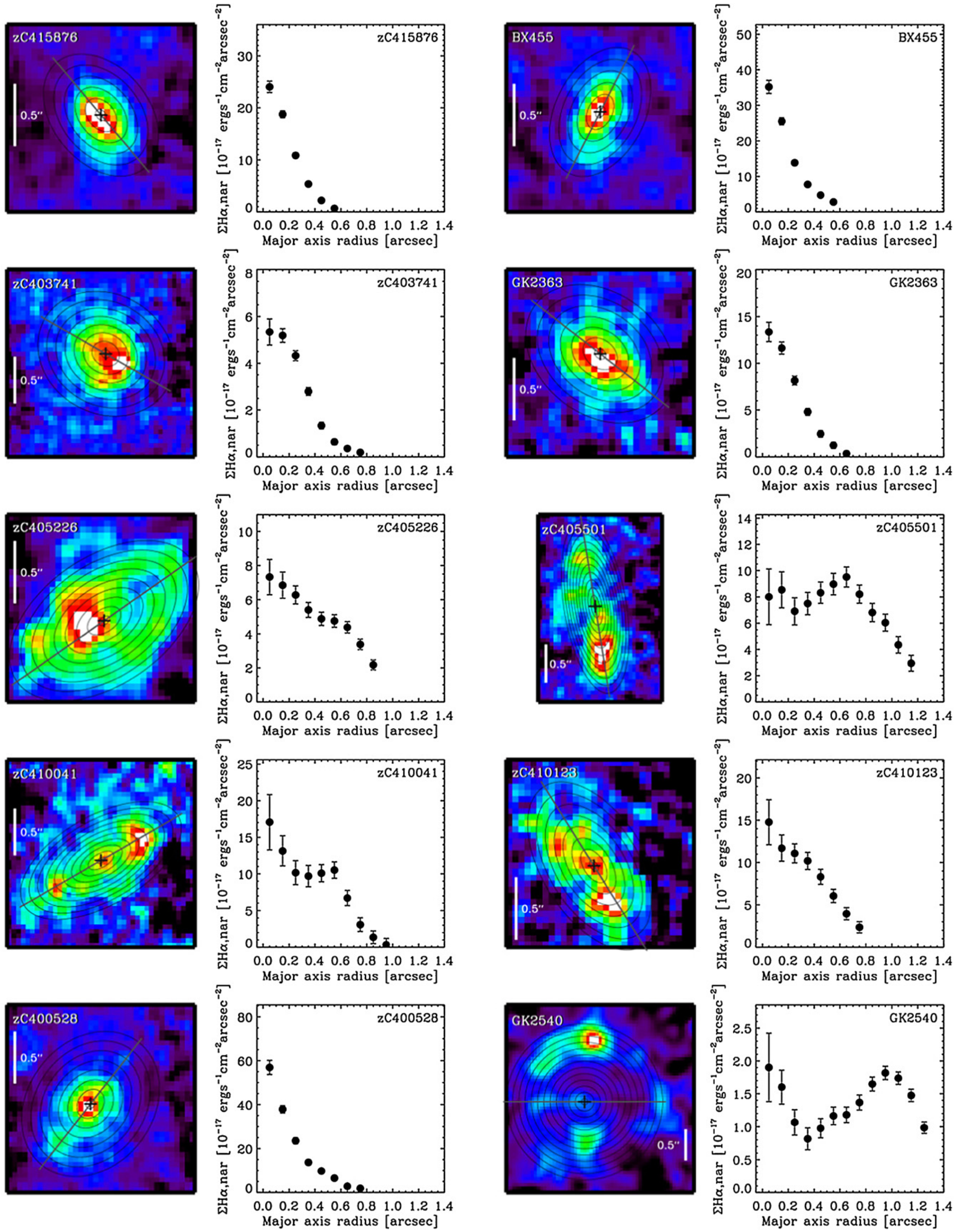

Figure 21. Hα surface brightness distributions for the 19 galaxies. For each galaxy, two panels show the two-dimensional surface brightness distribution of the (narrow component) Hα emission (extracted as described in Section 2.2) and the corresponding radial profile from the average surface brightness in elliptical annuli of width 0.″1. The elliptical annuli are indicated on the narrow Hα maps, are centered on the kinematic center (black cross) with P.A. equal to the kinematic major axis (black line), and with axis ratio matched to the observed outer narrow Hα isophotes.

(A color version of this figure is available in the online journal.)

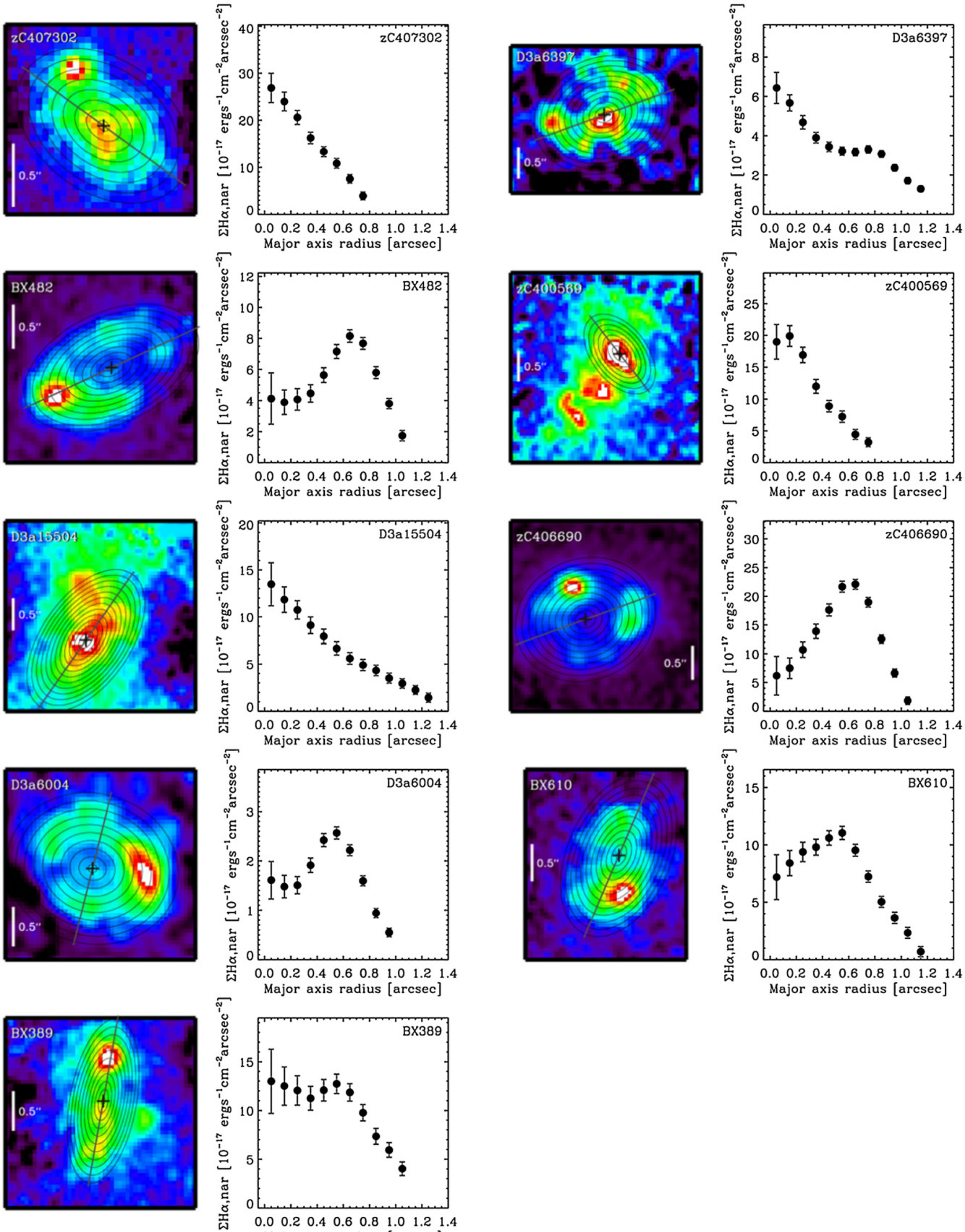

Figure 22. Same as Figure 21.
(A color version of this figure is available in the online journal.)

Calzetti modified screen approach probably breaks down for spatially resolved data (e.g., Genzel et al. 2013), since in reality the extinction is a combination of the large-scale dust distribution in the diffuse interstellar medium with local dust concentrations associated with the individual star-forming clouds (Nordon et al. 2013; Wuyts et al. 2013). The integrated Calzetti screen approach taken by necessity in this paper (for lack of spatially resolved A_V maps) probably underestimates molecular columns in the densest, dustiest star-forming clumps and in nuclear gas concentrations. To convert star formation surface densities obtained in this way to molecular gas surface densities, we used the PHIBSS calibration from Tacconi et al. (2013), based on galaxy integrated CO measurements in massive main-sequence SFGs between $z \sim 0$ and 2.5. PHIBSS yields a simple linear KS relation and a slowly varying depletion timescale, $M_{\rm mol\ gas}\ (M_\odot) = t_{\rm depl}(z) \times {\rm SFR}\ (M_\odot\ {\rm yr}^{-1})$, with $t_{\rm depl} = 1.5 \times 10^9\ (1{+}z)^{-1}$ (yr) (see also Saintonge et al. 2011, 2012, 2013). This calibration is probably fairly robust on galaxy integrated scales (Daddi et al. 2010a; Magdis et al. 2012; Magnelli et al. 2012), with a systematic uncertainty of ± 0.3 dex because of uncertainties in the CO to molecular gas conversion factor and in the SFRs. However, within galaxies the spatially resolved molecular KS relation may be steeper than linear, both in the local universe and at high z (Kennicutt et al. 2007; Daddi et al. 2010b; Heiderman et al. 2010; Kennicutt & Evans 2012; Genzel et al. 2013). For the $N \sim 1.3$ slope proposed by Kennicutt et al. (2007) in M51 ($N = \log\Sigma_{\rm SFR}/\log\Sigma_{\rm mol\ gas}$), for instance, such a non-linear relation would have the tendency of lowering the inferred molecular gas columns in the brightest star formation regions (by 60% over a factor of 10 in surface density), plausibly counteracting some of the extinction effects discussed above. The inferred major-axis, molecular surface density distributions for all of our 19 galaxies are shown in the lower right panels of Figures 2–20.

5. *Inferred Q-distribution*. We finally combined the information on σ_0 and $\kappa(R)$ from the kinematic modeling, with the gas distributions $\Sigma_{\rm mol\ gas}$ from the (narrow velocity width, after correction for broad emission; see above in point (4)) Hα data to infer the Toomre parameter for each pixel along the major axis, using Equation (2). Uncertainties in Q are derived from the pixel-by-pixel uncertainties in Σ. The uncertainties in σ_0 and κ are not included, as they mostly enter the larger systematic uncertainties but much less so the radial variations. Including these uncertainties would increase the average fractional error of Q from $\sim$0.15 to $\sim$0.4. The inferred major-axis Q-distributions for all of our 19 galaxies are shown in the lower right panels of Figures 2–20.
6. *Inferred stellar surface density distribution*. S. Tacchella et al. (in preparation) have analyzed J- and H-band WFC3 images of 13 of the 19 SFGs discussed in this paper and inferred intrinsic stellar mass surface density maps. From these maps we extracted the central values in the same apertures as for the "inner" molecular gas surface densities (typically with a radius of 0$''$.1–0$''$.15), to derive total inner (central) baryonic surface densities.

In Table 1 we summarize the inferred basic parameters, and in particular the dynamical mass and estimates of $\Sigma_{\rm mol\ gas}$ and Q for the "inner" (central 0$''$.1–0$''$.15 in radius) and "outer" regions in each galaxy. The latter is typically an average over 0$''$.2–0$''$.3, on either side of the nucleus and centered near $R_{1/2}$, or the ring maximum identified in the modeling.

3. RESULTS

3.1. More than Half of the SFGs Exhibit Hα Rings

Figure 23 compares the inferred major-axis, molecular gas surface density distributions (inferred from the Hα surface brightness distribution through the KS relation; see figure caption) of all 19 galaxies. As already stated in Section 2.2 (point (4)), the angle-averaged distributions in Figures 21 and 22 are very similar. A significant number of these distributions are not centrally peaked but exhibit an off-center peak (or at least an inflection point), that is, a radial ring in observed Hα light. More than half of our sample (at least 11, and perhaps as many as 13 of 19) require modeling with a ring component in Hα light, or have $\Sigma_{\rm outer}/\Sigma_{\rm inner} > 0.9$. The presence of bright, giant star-forming clumps in most of our galaxies (and in general in many $z \sim 2$ SFGs; Cowie et al. 1995; van den Bergh et al. 1996; Giavalisco et al. 1996; Elmegreen et al. 2004, 2009; Förster Schreiber et al. 2009, 2011a, 2011b; Barro et al. 2013) necessarily affects the inferred brightness distributions and radial cuts shown in Figure 23. However, the angle-averaged distributions shown in Figures 21 and 22 show that the impact of individual clumps is modest. In no case is the inference of a "ring" just the result of a single bright off-center clump. The Hα rings may represent either depressions of star formation surface density or peaks of extinction in the nuclear regions of these galaxies.

The ring fraction may increase with dynamical mass. When sorted by dynamical mass, seven to eight of the upper half of our sample (10) have rings, while only four to five of the lower mass half (nine) do. However, this conclusion needs to be taken with caution. In addition to the small sample size and resulting modest statistical significance that can be reached, the fraction of rings for lower mass galaxies (typically smaller radii) could be underestimated because of our instrumental resolution. In addition, the non-Gaussian AO point-spread function shape (with substantial wings on the seeing limited scale) will have the tendency to fill in a compact ring brightness distribution. An example is the central Hα compact disk in zC400569, which can be modeled well as an exponential (Figure 15). A close inspection of the major-axis position–velocity distribution and of the Hα surface brightness distribution (upper and lower right panels in Figure 15), however, suggests that the exponential disk has a small central hole. We count this galaxy as an "exponential" but list in Table 1 the possibility of a compact ring.

We have noted the occurrence of prominent Hα rings in several of the massive SFGs in the current sample before (BX 482, zC406690; Genzel et al. 2008, 2011). The present study shows that such rings are likely common in massive high-z star-forming disks. Wuyts et al. (2013) have investigated 473 3D-*HST* galaxies between $z = 0.7$ and 1.5, taking advantage that for this survey (Brammer et al. 2012) both Hα and stellar surface densities are available at *HST* resolution ($\sim$0$''$.2). Wuyts et al. (2013) find from stacked light distributions that there is a clear trend toward a nuclear depression in Hα equivalent width. Nelson et al. (2013) find that these depressions become more prominent in larger, more massive systems. The work of Wuyts and coworkers is in excellent agreement with our findings.

An immediate question is whether these central depressions in the Hα distributions are intrinsic or whether they might be caused by differential extinction in flat or even centrally

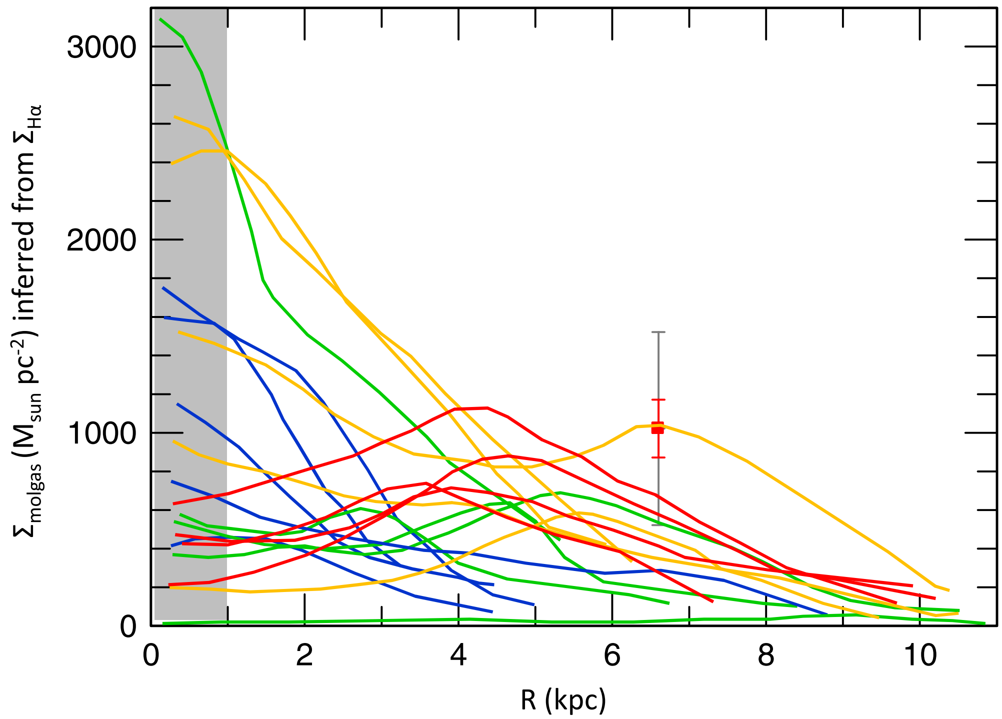

Figure 23. Inferred radial molecular gas surface density distributions for the 19 SFGs in this paper. The molecular gas masses and column densities (including a 36% correction for He) are inferred from the observed Hα surface brightness major-axis cuts at a typical FWHM resolution of $\sim$2 kpc (averaging the values on either side of the center), corrected for global extinction with a "double"-Calzetti recipe, then converted to SFR surface density with the standard conversion factor of Kennicutt (1998a, 1998b; but for a Chabrier IMF), and finally converted to molecular column density with the Tacconi et al. (2013) calibration from PHIBSS, as described in Section 2.2 (point (4)). The 19 SFGs are marked by different colors in four bins of dynamical mass. Blue denotes the five SFGs with masses of $10.36 \leqslant \log M_{\rm dyn} \leqslant 10.5$, green masses of $10.68 \leqslant \log M_{\rm dyn} \leqslant 10.93$, orange masses of $11.04 \leqslant \log M_{\rm dyn} \leqslant 11.28$, and red masses of $11.34 \leqslant \log M_{\rm dyn} \leqslant 11.41$. Typical statistical (red) and systematic (gray) uncertainties are indicated. The appearance of ring distributions, especially among the two highest masses, is apparent. The bottom green curve is GK 2540. The gray-shaded area on the left denotes the radius regime that is below the average HWHM instrumental resolution, and thus represents a somewhat uncertain inward extrapolation.

(A color version of this figure is available in the online journal.)

peaked intrinsic surface brightness distributions. The differential extinction hypothesis may be supported by the fact that in our sample, SFGs with rings have an average Hα surface brightness 0.5–0.6 dex lower than in the centrally peaked cases. However, the much less extinction-sensitive, Hα equivalent width in the stacked light distribution of the 473 $z = 0.7$–1.5 SFGs studied by Wuyts et al. (2013) exhibits a central depression of 0.3–0.4 dex relative to the surrounding disk as well. Wuyts et al. (2013) also consider differential extinction between the R-band stellar light and Hα emission and correct the Hα emission appropriately, in the spirit of Calzetti et al. (2000), but considering physical extinction models better reproducing the rest-UV and Hα data of their 3D-*HST* high-z SFG sample. Even after such a correction, the central Hα equivalent width depressions in the stacked light distribution remain, albeit at a smaller amplitude of 0.2–0.25 dex relative to the surrounding disk.

The work of Wuyts et al. (2013), Nelson et al. (2013), and E. J. Nelson et al. (in preparation) suggests that differential extinction gradients and central gas/dust concentrations are probably present and need to be taken into account. Correction for extinction decreases the amplitudes of the rings but does not seem to remove them. The rings are probably an intrinsic property of the star-forming gas.

3.2. *Q-distributions Are Centrally Peaked*

Figure 24 compares the inferred major-axis Q-cuts for the 19 galaxies. In contrast to the observed Hα distributions and inferred molecular gas surface density distributions, the Q-distributions in all of our 19 SFGs are centrally peaked. With modest extrapolation to the spatial scales below the half-width at half-maximum (HWHM) resolution (gray shaded region in Figure 24), 13 of the 19 SFGs exhibit $Q_{\rm inner} \geqslant 1.3 \sim Q_{\rm crit}$ (thick disk, $f_{\rm gas} \sim 0.5$). In the framework of the stability theory of rotating disks discussed in the Introduction, the nuclear regions would be globally stable to large-scale, gravitational fragmentation. All but one of the 19 SFGs have Q significantly below unity in the outer parts and ring regions, fully consistent with the global/violent disk instability scenario, as shown previously by Genzel et al. (2011) for a subset of four of our SFGs.

The Toomre parameter is inversely proportional to gas surface density, so naturally the question arises whether the centrally peaked Q-distributions are merely the consequence (and possibly an artifact) of the central minimum in the observed Hα distributions (used to infer gas surface density). This question is explored in Figure 25, where we show again in the left panel the pixel-by-pixel Q-distributions of all 19 SFGs, as in Figure 24, with the $\kappa(R)$ distributions obtained from the kinematic models, and the obvious strong trend of negative radial Q-gradients. To explore the dependence of the Q-gradients on gas surface density and κ-distributions independently, in the central panel of Figure 25 we replaced the κ distributions by a single average value for each galaxy. Now the gradients disappear for most points. Again with modest extrapolation to the radial scales below our resolution, $Q_{\rm inner}$ remains greater than unity for much

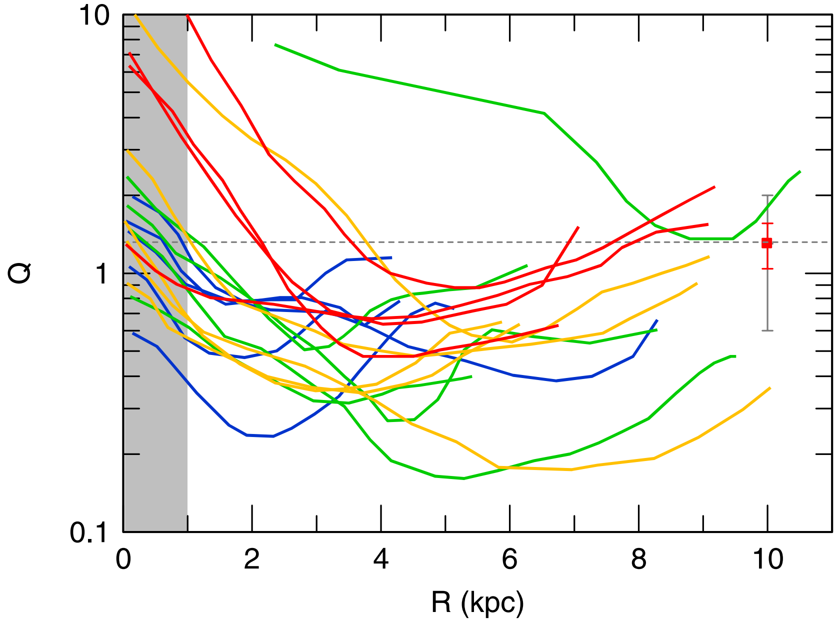

Figure 24. Radial distributions of the Toomre Q-parameter for the 19 SFGs in this paper, separated as in Figure 23 by dynamical mass in the lowest five (blue: $10.36 \leqslant \log M_{\rm dyn} \leqslant 10.5$), next five (green: $10.68 \leqslant \log M_{\rm dyn} \leqslant 10.93$), next five (orange: $11.04 \leqslant \log M_{\rm dyn} \leqslant 11.28$), and highest bins (red: $11.34 \leqslant \log M_{\rm dyn} \leqslant 11.41$). Typical statistical (red) and systematic (gray) uncertainties are indicated. The dashed horizontal line marks $Q_{\rm crit} = 1.3$ for a thick gas-rich disk with $f_{\rm gas} \sim 0.5$. The gray shaded area on the left denotes the radius regime that is below the average HWHM instrumental resolution, and thus represents a somewhat uncertain inward extrapolation.

(A color version of this figure is available in the online journal.)

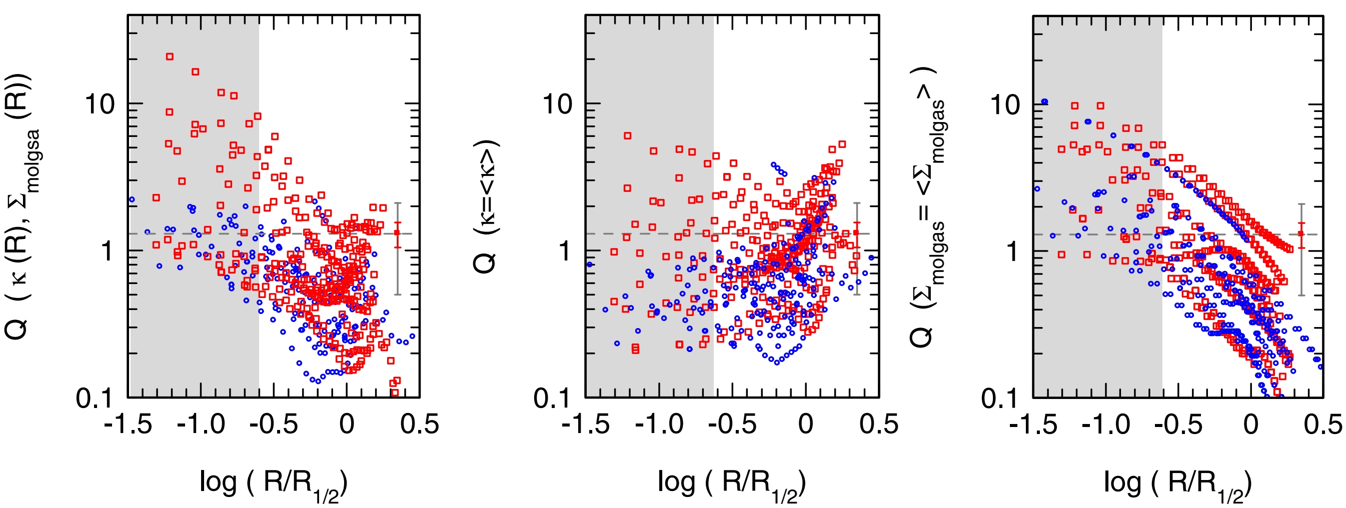

Figure 25. Distribution of Q-values for each pixel and all SFGs, separated in two mass bins (blue: 11 lowest mass; red: 8 highest mass). The left panel depicts the same data as in Figure 24, with $\Sigma_{\rm mol\ gas}$ derived from the Hα data, and $\kappa(R)$ and σ_0 derived from the dynamical modeling. The central panel again uses the same molecular surface densities and velocity dispersions as the right bin but instead applies a constant average $\langle\kappa\rangle$ value for each galaxy. The right panel instead uses $\kappa(R)$ and a constant (median) value for the molecular surface densities. A comparison of the three panels shows that the strong dichotomy of strongly gravitationally unstable ($Q < 1$) gas in the outer disks and stable ($Q > 1.3$) gas in the nuclear regions, especially for the more massive SFGs, is more driven by the radial variation in κ than in $\Sigma_{\rm mol\ gas}$. The red and gray error bars denote the typical statistical and systematic uncertainty of the data. The gray shaded area in each panel denotes the radius regime that is below the average HWHM instrumental resolution, and thus represents a somewhat uncertain inward extrapolation.

(A color version of this figure is available in the online journal.)

of the high-mass half of the SFGs, but so does $Q_{\rm outer}$. If that were the answer, one would have to doubt the relevance of the stability theory, or our calibration of the Q-values, since obviously active star formation does occur throughout the outer ring structures of these massive galaxies.

Finally, in the right panel we let κ vary with R, as in the left panel, but now use a flat $\Sigma_{\rm mol\ gas}$ distribution for each galaxy, so that there are no central depressions. While the outer Q-values are now somewhat higher, the inner values and especially the radial trends are pretty much the same as in the left panel. Figure 25 thus shows that it is the radial variations in κ, and not in $\Sigma_{\rm mol\ gas}$, that largely drive the strong central Q-peaks in the massive half of the population. The κ distributions in many of our SFGs increase strongly toward the center, $\kappa \sim 1/R$, because of the fairly flat or even inward rising rotation curves to 2–3 kpc (central upper panels in Figures 2–20).

We conclude that the centrally peaked Q-distributions are influenced, but not dominated, by the Hα ring distributions and

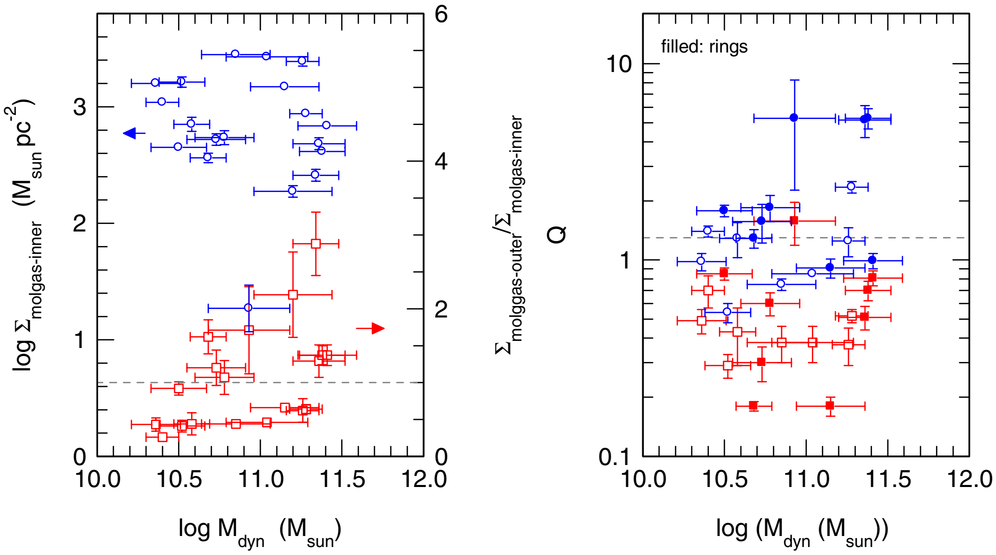

Figure 26. Evidence for radially quenching of gravitational fragmentation in $z \sim 1.5$–2.5 disks. The left panel shows the central molecular gas surface densities (blue circles, left axis) and the ratio of average outer disk (near $R_{1/2}$, or the ring maximum) to central surface densities (red squares, right axis), as a function of dynamical mass. The right panel shows the inner (blue circles) and outer (red squares) average values of the Q-parameter as a function of dynamical mass. Ring galaxies ($\Sigma_{\rm molgas}$(inner)/$\Sigma_{\rm molgas}$(outer) > 0.9) are denoted by filled symbols. As before, the molecular gas column densities (including a 36% correction for He) are inferred from the observed Hα surface brightness major-axis cuts at a typical FWHM resolution of ~2 kpc (averaging the values on either side of the center), corrected for global extinction with a "double"-Calzetti recipe, then converted to SFR surface density with the standard conversion factor of Kennicutt (1998a, 1998b, but for a Chabrier IMF), and finally converted to molecular column density with the Tacconi et al. (2013) calibration from PHIBSS, as described in Section 2.2 (point (4)).

(A color version of this figure is available in the online journal.)

are mainly driven by central mass concentrations increasing the central shear in the rotation curves.

3.3. Rings, Central Q-peaks, and Inside-out Quenching

Assuming now that the inferred $\Sigma_{\rm mol\ gas}$ and Q-distributions are a fair representation of reality, Figure 26 explicitly shows the dependence of Hα and Q-distributions on galaxy (dynamical) mass. This figure summarizes and strengthens the main results touched on before. The Q-values in the outer parts of the high-z disks in our sample, at all masses, are consistent with being globally unstable to gravitational instability up to the Toomre scale. The lower mass disks are also near the critical Q-value in their inner parts, consistent with their largely flat or even centrally peaked star formation distributions. However, strong mass concentrations inferred from the kinematics and rings in Hα drive the *central* Toomre parameters above unity in more than half of the galaxies.

The presence of star-forming rings and high central Q-values appear to be correlated with each other, as well as with dynamical mass. Quantitatively, of the 10 rings with $\Sigma_{\rm molgas}$(inner)/$\Sigma_{\rm molgas}$(outer) $\geqslant 0.9$, 9 have $Q_{\rm inner} \geqslant 1.3$, and of the 13 galaxies with $Q_{\rm inner} \geqslant 1.3$, 9 are rings (Figure 26). The average central Q-value (and its 1σ uncertainty) of the 11 robust Hα rings is $\langle Q_{\rm inner}\rangle = 3.9$ (±1), while the 8 exponential distributions have $\langle Q_{\rm inner}\rangle = 1.2$ (±0.2). The difference is significant at the 2.6σ level (~1% probability of being drawn from distributions with the same mean). Large central Q-values and the radii of the Hα rings also show a modestly significant dependence on dynamical mass. Dividing our sample into the lower (9 SFGs) and upper mass (10 SFGs) halves, the average inner Q-values (and their 1σ uncertainties) are 1.3 (±0.13) and 4.1 (±1.1). For the ring radii the averages are 3.2 (±0.8) and 5.6 (±0.6) kpc. All these differences are significant at the 2.5σ–3σ level, indicating a ~1% probability of being drawn from distributions with the same mean.

One of our galaxies, GK 2540, is an interesting special case. This system has relatively low mass (log$M_* = 10.3$), with little evidence for a prominent central stellar mass concentration (Kurk et al. 2013). Its location below the main sequence means that this galaxy has less gas than the average galaxy at that mass (Magdis et al. 2012; Tacconi et al. 2013). GK 2540 exhibits very low star formation and gas column densities (Figures 11 and 21), with Q barely dropping to unity in a very large, narrow star-forming ring. GK 2540 thus may be a case where the lack of star formation throughout the disk is largely driven by the lack of gas, perhaps as the result of currently low accretion, driving the galaxy below the main-sequence line.

In summary, the data in the 19 rotation-dominated SFGs studied in this paper are consistent with the hypothesis presented in Section 1 that the global gravitational instability over time is suppressed from the inside out. As the galaxies grow in mass, global gravitational collapse, cloud formation, and plausibly star formation are shut down over an increasing area of the most massive disk galaxies. Given that we see $Q_{\rm inner} > Q_{\rm crit}$ in about half of our massive SFGs, the gravitational quenching mechanism may be quite efficient and may have a high duty cycle.

3.3.1. Is there Evidence for Lower Efficiency Star Formation?

An obvious next question is whether the galaxy-wide SFR in the Q-excess/ring galaxies is actually suppressed below that expected from the cold gas reservoir? For a clean test one would need direct estimates of the molecular gas masses of our sample for determining the gas depletion timescales (e.g., from CO observations; see Tacconi et al. 2010, 2013; Daddi et al. 2010b; Genzel et al. 2010). Such data are unfortunately not yet available at high z. Saintonge et al. (2012) do find a modest increase of depletion timescales below the main sequence for their Sloan Digital Sky Survey based $z \sim 0$ COLDGASS CO survey. Indirect evidence may come from the fact that the

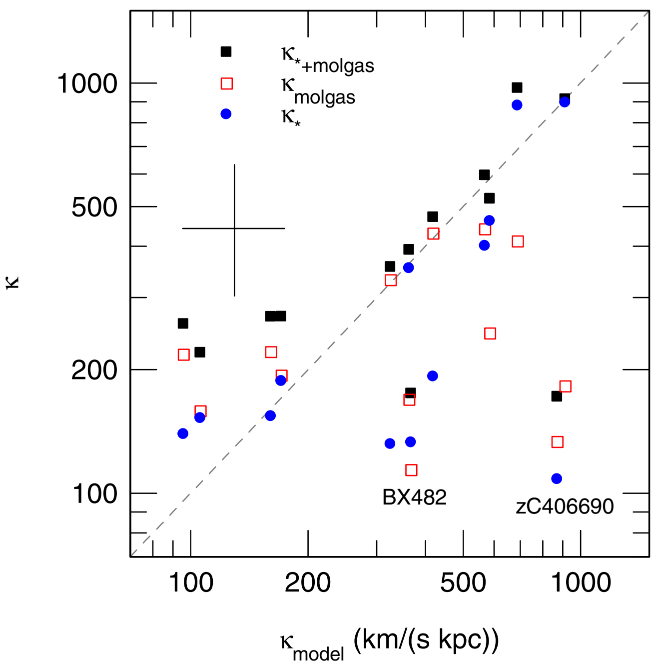

Figure 27. Comparison of the epicyclic frequency determined from the dynamical modeling (horizontal axis) with the epicyclic frequency determined from the observed central stellar mass surface density (filled blue circles), from the inferred molecular gas surface density (open red squares), as well as their sum (filled black squares) on the vertical scale. The fiducial radius at which this comparison is made is 0''.05 (0.4 kpc). Given the estimated systematic uncertainties (large black cross), the combination of gas and stellar mass can plausibly account for the central mass inferred from the gas kinematics (the dashed gray line indicates a ratio of unity), with the exception of the two "dark centered" galaxies BX 482 and zC406690. The central shear is dominated by gas for the galaxies with low shear, and with the exception of BX 482 and zC406690, there is a tendency for the stellar component to become dominant for the higher κ systems.

(A color version of this figure is available in the online journal.)

main-sequence relation between stellar mass and SFR does not have a constant slope but flattens at high stellar mass, at all redshifts between ∼0 and 2.5 (Whitaker et al. 2012). The ratio of sSFRs at $\log M_* = 10$ to $\log M_* = 11$ (in the regime where most of our rings are) is ∼2, and increasing from high to low redshift. This drop may indicate that the higher mass galaxies on average have lower molecular gas fractions, or that they form stars less efficiently than the lower mass galaxies at the same redshift. This difference can also be seen for our own sample when comparing the location of the galaxies relative to the slope 1 main-sequence line in Figure 1. A more unambiguous test from CO observations at $z \sim 1$–2 is planned as part of the PHIBSS2 survey on the IRAM Plateau de Bure Interferometer (PdBI).

3.4. What is the Nature of the Central Mass Concentrations?

What is the nature of the central mass concentrations inferred from our dynamical modeling? In Figure 27 we compare the nuclear κ-values inferred from the kinematic modeling on the horizontal axis with the nuclear κ-values obtained from the stellar mass distribution (filled blue circles; S. Tacchella et al. in preparation), from the molecular mass distribution (open red squares), and from the total (stellar + gas) mass distribution (filled black squares) on the vertical axis, for the 13 galaxies where both are available. Here we extrapolated the data and modeling inward to a fiducial radius of 0.4 kpc, but choosing a larger radius does not change the result. Given the substantial systematic uncertainties, the data for 11 of the 13 galaxies are in very good agreement with the hypothesis that the mass concentration inferred from our dynamical modeling is the same as the sum of cold (star-forming) gas (inferred from the Hα brightness distribution) and stars (as estimated from the *HST* data). The ionized gas contributes only about 3%–10% of gas mass (Genzel et al. 2011). There is an additional substantial contribution from atomic hydrogen, but at the typical column densities and pressures inferred from the molecular column densities most of the cold gas should be in molecular form (Blitz & Rosolowsky 2006).

In the galaxies with low $\kappa_{\rm model}$ (largely identical with the galaxies with low dynamical masses), the central mass is dominated by gas. For the higher $\kappa_{\rm model}$ galaxies (mostly higher mass), the fraction of stellar mass contributing to the central mass concentration becomes significant or dominant. As we have shown in the last section, large central κ-values are the main drivers for the supercritical Q-values. Figure 27 suggests that the large central κ-values in turn are driven by the emergence of massive stellar bulges.

There are two outliers (BX 482 and zC406690) where the dynamical modeling indicates the presence of much more mass than can be explained by either stars or molecular gas. These galaxies show very prominent Hα and stellar rings, with little emission coming from the center, yet the kinematics indicates a major central mass concentration (Figures 14 and 17). One would have to resort to postulating either a concentration of sterile, non-star-forming gas there, or very large nuclear extinction, or a combination of both. However, Tacconi et al. (2013) have reported direct CO 3–2 observations for both galaxies, which yield no or only faint CO emission. Assuming a Galactic conversion factor, the faintness of the millimeter line emission is even inconsistent with the KS estimate from Hα used in this paper, and certainly would not suggest extra gas (and dust). Given the low metallicity of both systems, it is possible in these two cases that much of the molecular gas is "CO-dark" due to UV photodissociation (Wolfire et al. 2010; Genzel et al. 2012). These two "dark" rings are currently not understood.

3.5. Caveats and Alternatives

As pointed out in the earlier sections, the conclusions in this paper, in addition to relying on a relatively small statistical sample, rest on a number of assumptions, all of which are uncertain or might be challenged.

1. The extinction correction of the Hα surface brightness maps relies on a uniform foreground screen model across each galaxy with extra attenuation toward H II regions relative to stars as proposed by Calzetti et al. (2000). This assumption (Calzetti et al. 2000; Calzetti 2001) does empirically work remarkably well even in very extreme, dusty local starburst regions in the local universe, including ultraluminous infrared galaxies (Calzetti et al. 2000; Calzetti 2001; Engel et al. 2010, 2011). Yet it is unlikely to be applicable to spatially resolved data (Genzel et al. 2013; Nordon et al. 2013; Wuyts et al. 2013). Moreover, the assumption of constant extinction across galaxies, even on resolved scales of ∼1–2 kpc, is unrealistic. Local starburst galaxies, for instance, typically have extinctions peaking in the nuclear regions. As such, the data for our sample cannot exclude the possibility that the observed Hα ring structures are caused, or at least strongly influenced, by nuclear dust concentrations. In fact, a high-resolution CO 3–2 IRAM

PdBI map of one of the most massive SFGs in our sample, Q2343-BX 610, indeed exhibits such a nuclear gas/dust concentration (Tacconi et al. 2013). However, the analyses of Wuyts et al. (2013) and Nelson et al. (2013), based on a much larger 3D-*HST* sample of $z \sim 1.5$ main-sequence SFGs, suggest that the radial trends in the Hα versus stellar light/mass distributions are unlikely to be entirely caused by radial variations in extinction. This is probably the result of the clumpy distribution of the dust in the "birth clouds" (Wuyts et al. 2013). The maximum dust columns in these birth clouds can be large, $A_V \sim 50$–100. However, because of the clumpiness of the cold gas and dust, the effective extinction averaged over kpc scales is $A_{V,\mathrm{eff}} \leqslant$ a few so that radiation in the optical band can still escape (Genzel et al. 1998, 2013).

2. The empirical near-linear "molecular KS relation" that appears to hold on galaxy integrated and large scales in local and $z \sim 1$–2 main-sequence SFGs (Bigiel et al. 2008; Leroy et al. 2008, 2013; Genzel et al. 2010; Saintonge et al. 2012; Tacconi et al. 2013; Daddi et al. 2010b) might break down on sub-galactic scales, in part because of the issue of extinction correction above (Genzel et al. 2013), and in part because of sampling and evolutionary effects (Onodera et al. 2010; Schruba et al. 2010; Calzetti, Liu, & Koda 2012). Fortunately, points (1) and (2) to some extent counteract each other in the analysis of the current data.
3. The assumption of a constant local velocity dispersion in our modeling may be too simplistic, although the best current empirical evidence at both low and high z is in support of just such a constant dispersion "floor" (Heyer & Brunt 2004; Genzel et al. 2011; Davies et al. 2011; FS14; but see Green et al. 2010; Swinbank et al. 2012; Wisnioski et al. 2012). Specifically relevant to our study is the work of Genzel et al. (2011) and FS14, who searched for variations in σ_0 toward bright star-forming clumps in $z \sim 2$ SFGs in residual velocity dispersion maps, after correction for beam-smeared rotation. They did not find any significant variations with local star formation surface density, with the possible exception of some nuclear regions, where the velocity dispersions appear to increase, most likely because of poorly modeled and unresolved nuclear motions. If these velocity dispersion increases in the central regions were real and intrinsic, however, this would thus further increase Q and strengthen the results discussed above.
4. Our kinematic/mass modeling delivers plausible but not unique model parameters and relies on the assumption of equilibrium kinematics, which may not be justified in some cases. For instance, polar mergers may cause collisional ring galaxies (see D'Onghia et al. 2008). In fact, one of our two "dark centered" rings above the main sequence, BX 482, has a nearby smaller companion about 3″ to the southeast and redshifted by about 750 km s^{-1} relative to the main galaxy. The companion is a compact SFG that is bright in Hα (and CO; Tacconi et al. 2013). It is possible that in this case, the ring structure is a non-equilibrium result driven by a galaxy collision.
5. If the molecular gas depletion timescale were not constant but proportional to the local dynamical timescale, ring structures may naturally form as a result of this radial dependence, rather than from gravitational quenching. Future high-resolution molecular observations of our SFGs will be able to test such a hypothesis. There is no dependence of the depletion timescale on galactic radius in $z \sim 0$ star-forming disks (Leroy et al. 2008, 2013).

3.6. Comparison to Low-z Disk Galaxies

In contrast to the situation discussed here for high-z star-forming disks, recent observations of massive ($\log M_* > 10$) $z \sim 0$ SFGs suggest that the Toomre parameter does not play a major role in controlling galactic star formation on large scales. In the HERACLES CO 2–1 survey at the IRAM 30 m telescope (in combination with *Galaxy Evolution Explorer* UV data, SINGS/*Spitzer* 24 μm data, and THINGS H I data) Leroy et al. (2008) have carried out spatially resolved (400–800 pc resolution) mapping of the gas–star formation relation in 12 massive spirals ($\log M_* = 10.1$–10.9) and 11 dwarfs ($\log M_* = 7.1$–9.9). From these data Leroy et al. construct the radial dependence of the Q-parameter (in gas as well as gas + stars). Their Figure 9 (equivalent to our Figure 24) does not show any strong trends of Q_{gas} or $Q_{\mathrm{gas+*}}$ with galactocentric radius. The average massive spiral at $z \sim 0$ has $Q \sim 2$–4 throughout its disk and nuclear regions and thus is stable against gravitational fragmentation on large scales potentially influenced by rotational shear. The galactic gas depletion timescale (the inverse of the "star formation efficiency") does not vary with Q.

A particularly instructive case is the grand design spiral M51 (NGC 5194), which has become a benchmark system for studying star formation on galactic scales. Hitschfeld et al. (2009) show that Q_{gas} and $Q_{\mathrm{gas+*}}$ on average range between 2 and 4 throughout the disk of M51, but dip to values near or even slightly below 1 on the spiral arms in the outer disk. However, the gas depletion timescale in these arms does not differ from the interarm regions; strong spiral arms may have $Q \leqslant Q_{\mathrm{crit}}$ but do not result in more efficient star formation (Foyle et al. 2010). Elmegreen (2011) concludes that "the primary effect of a spiral is to concentrate the gas in the arms without changing the SFR per unit gas." In the analysis of the first CO 1–0 IRAM PdBI observations of M51 within the PAWS high-resolution program Meidt et al. (2013) even conclude that in those parts of the spiral arms with strong streaming motions and large pressure gradients, giant molecular clouds (GMCs) may actually be driven to lower star formation efficiency. Spiral arms may thus act on the one hand to collect and form GMCs and on the other also to decrease their star formation efficiency.

Q scales with the product of $\kappa\ \sigma_0\ \Sigma_{\mathrm{molgas}}{}^{-1}$. The difference between the Q-values in high- and low-z SFGs depends on all three quantities, but the data of Hitschfeld et al. (2009) suggest that the much lower gas columns in M51 as compared to our high-z SFGs are the main driver for the higher Q-values of that system. Gravitational disk instability dominates cloud formation and star formation in the high-z systems, while in local universe galaxies the shepherding of gas by spiral arms and non-circular streaming are more important.

3.7. Comparison to Theoretical Expectations

As we have discussed in Section 1, the occurrence of star-forming rings in galaxies with high central Q-values would be a natural outcome of quenching of radial gas transport into the inner disk regions. As Q is below unity in the outer regions, gravitational torques and clump–clump interactions should lead to angular momentum redistribution, driving angular momentum outward and gas inward. If the inspiraling material is gas rich, that is, if the star formation timescale is longer than the in-fall timescale (Dekel & Burkert 2014), the gas should reach the inner region where the disk is stable due to $Q > 1$ and where radial transport should be suppressed. At the boundary between the gravitationally stable inner region and the unstable outer region the in-falling gas may accumulate, generating a gas-rich ring with enhanced star formation. Star-forming rings driven by the combined effect of gravitational instability and radial gas transport indeed occur frequently in recent cosmological galaxy formation hydro-simulations with sufficient resolution to study sub-galactic scales, and they are more common in more massive systems (Ceverino et al. 2010; Genel et al. 2012; D. Ceverino 2013, private communication).

What happens to the "sterile" gas collecting in the inner regions? Will it not accumulate there until Q drops again sufficiently to rekindle the instability? In the theoretical studies of these processes the radial transport becomes inefficient at the same time as the gravitational instability stops, drastically decreasing the matter transport into the center (Martig et al. 2009; Ceverino et al. 2010; Cacciato et al. 2012; Forbes et al. 2013). During that phase, star formation continues in the central regions at a lower rate. Thus, there may be little accumulation. Alternatively, AGN feedback may efficiently eject gas that is transported into the nuclear regions.

Why do the massive galaxies especially have large bulge masses with star-formation-quenched inner regions and rings? It is tempting to identify these galaxies as being in their last active phase of star formation. Gas in their inner regions has already been depleted by star formation with refueling through radial inflow from the outer, gas-rich disk regions being suppressed as discussed above. The fact that most of the massive rings in Figure 1 (with the exception of the "dark rings" BX 482 and zC406690; see Section 3.4) are somewhat below the main-sequence line may also suggest that gas refueling by infall from the cosmic web has slowed down and that these galaxies are in the process leaving the main sequence with their SFR decreasing. Adopting SFR $= M_{\rm mol\ gas}/t_{\rm depl}$, the gas mass in this final phase is expected to decrease exponentially with an e-folding timescale of $t_{\rm depl} \sim 1$ Gyr. A change in the SFR by 0.3 dex (as in Figure 1) then corresponds to an evolutionary timescale comparable to the depletion timescale, which would appear reasonable.

4. CONCLUSIONS

We have presented high-quality AO assisted SINFONI/VLT IFU spectroscopy of Hα line emission and kinematics in 19 rotation-dominated, well-resolved (and thus relatively large), near-main-sequence SFGs, ranging in stellar mass from 4×10^9 to $3 \times 10^{11}\,M_\odot$.

We have used the kinematic information in these data sets to deduce the dependence of circular velocity, dynamical mass, and epicyclic frequency as a function of major-axis offset from the dynamical center, as well as the local velocity dispersion in the outer parts of these galaxies. We have taken the Hα surface brightness distributions, corrected globally for extinction, together with the $z \sim 2$ PHIBSS calibration of the molecular KS relation (Tacconi et al. 2013), to construct proxies of the molecular column density maps. Combining kinematic modeling and Hα mapping, we were then able to derive major-axis cuts of the Toomre Q-parameter for all 19 SFGs in our sample.

We find that in all of our galaxies Q decreases from the inside out, where it is substantially below unity. All outer disks thus appear to be globally unstable to gravitational fragmentation. In contrast, the Q-value near the center, $Q_{\rm inner}$, increases above the critical value of about 1.3 for half to two-thirds of our sample. At the same time, a similar fraction of our galaxies exhibit Hα rings, rather than centrally peaked Hα distributions. The presence of ring structures and $Q_{\rm inner} \geqslant Q_{\rm crit}$ is correlated at the 99% probability level, and at a similar confidence level the value of $\langle Q_{\rm inner}\rangle$ increases with dynamical mass. The presence of rings and supercritical Q-values may be correlated with the emergence of massive central stellar bulges and a drop in the sSFR. Keeping in mind the modest sample size, and the uncertainties and possible pitfalls in our analysis, such unmodeled extinction gradients, radial variations in velocity dispersion, and departures from linearity in the relationship between star formation and molecular gas surface density, our findings are in plausible agreement with an efficient inside–out, low- to high-mass suppression/reduction of the gravitational instability in $z \sim 2$ SFGs that has been predicted by several recent theoretical papers. However, definite proof of the operation of the morphological quenching process at high z will require high-resolution maps of molecular column densities with millimeter interferometry.

We find that the supercritical central Q-values are mainly the consequence of the inferred intrinsic rotation curves to stay relatively flat, or even to rise, from the outer disks to the central few kpc. In 11 of the 13 SFGs in our sample with *HST* WFC3 imagery, the mass concentrations inferred from our modeling are consistent with the sum of the molecular gas and stellar mass near the centers. The central molecular mass concentrations dominate for the low dynamical mass galaxies of our sample, while the stellar contribution becomes significant and even dominant in all but two of the high-mass systems. This finding is consistent with the current theoretical picture that gas and newly formed stars in the gas-rich high-z disks are efficiently driven inward by torques and dynamical friction and establish a fast-growing star-forming bulge there.

The gravitational quenching process discussed above is unlikely to lead by itself to the long-term quenching of star formation but probably requires the participation of other players, such as the decrease of gas accretion rates with halo mass and cosmic time, and the removal of non-star-forming gas by feedback processes, such as AGN-driven nuclear winds.

We thank the staff of Paranal Observatory for their support. We are grateful to Daniel Ceverino for comments on the paper and for communicating to us the frequency of star-forming rings in his hydro-simulations. We thank Adam Leroy, Eva Schinnerer, Andreas Schruba, and Fabian Walter for comments on the Q-parameter in $z \sim 0$ disks. We also thank the referee for suggestions that helped improve the quality of the paper.

REFERENCES

Agertz, O., Teyssier, R., & Moore, B. 2009, MNRAS, 397, L64
Barro, G., Faber, S. M., Pérez-González, P. G., et al. 2013, ApJ, 765, 104
Bauermeister, A., Blitz, L., Bolatto, A., et al. 2013, ApJ, 768, 132
Bigiel, F., Leroy, A., Walter, F., et al. 2008, AJ, 136, 2846
Binney, J., & Tremaine, S. 2008, Galactic Dynamics (2nd ed.; Princeton, NJ: Princeton Univ. Press)
Blitz, L., & Rosolowsky, E. 2006, ApJ, 650, 933
Bonnet, H., Abuter, R., Baker, A., et al. 2004, Msngr, 117, 17
Bouché, N., Dekel, A., Genzel, R., et al. 2010, ApJ, 718, 1001
Bournaud, F. 2010, in ASP Conf. Ser. 423, Galaxy Wars: Stellar Populations and Star Formation in Interacting Galaxies, ed. B. Smith et al. (San Francisco, CA: ASP), 177
Bournaud, F., Elmegreen, B. G., & Elmegreen, D. M. 2007, ApJ, 670, 237
Bournaud, F., Elmegreen, B. G., & Martig, M. 2009, ApJL, 707, L1
Bower, R. G., Benson, A. J., Malbon, R., et al. 2006, MNRAS, 370, 645
Brammer, G. B., van Dokkum, P. G., Franx, M., et al. 2012, ApJS, 200, 13

Brooks, A. M., Governato, F., Quinn, T., Brook, C. B., & Wadsley, J. 2009, ApJ, 694, 396
Cacciato, M., Dekel, A., & Genel, S. 2012, MNRAS, 421, 818
Calzetti, D. 2001, PASP, 113, 1449
Calzetti, D., Armus, L., Bohlin, R. C., et al. 2000, ApJ, 533, 682
Calzetti, D., Liu, G., & Koda, J. 2012, ApJ, 752, 98
Carollo, C. M., Scarlata, C., Stiavelli, M., Wyse, R. F. G., & Mayer, L. 2007, ApJ, 658, 960
Ceverino, D., Dekel, A., & Bournaud, F. 2010, MNRAS, 404, 2151
Chabrier, G. 2003, PASP, 115, 763
Cowie, L. L., Hu, E. M., & Songaila, A. 1995, AJ, 110, 1576
Cresci, G., Hicks, E. K. S., Genzel, R., et al. 2009, ApJ, 697, 115
Daddi, E., Bournaud, F., Walter, F., et al. 2010a, ApJ, 713, 686
Daddi, E., Dickinson, M., Morrison, G., et al. 2007, ApJ, 670, 156
Daddi, E., Elbaz, D., Walter, F., et al. 2010b, ApJL, 714, L118
Davé, R., Finlator, K., & Oppenheimer, B. D. 2011, MNRAS, 416, 1354
Davé, R., Finlator, K., & Oppenheimer, B. D. 2012, MNRAS, 421, 98
Davies, R. I., Förster Schreiber, N. M., Cresci, G., et al. 2011, ApJ, 741, 69
Dekel, A., & Birnboim, Y. 2006, MNRAS, 368, 2
Dekel, A., Birnboim, Y., Engel, G., et al. 2009a, Natur, 457, 451
Dekel, A., & Burkert, A. 2014, MNRAS, 438, 1870
Dekel, A., Sari, R., & Ceverino, D. 2009b, ApJ, 703, 785
Dekel, A., Zolotov, A., Tweed, D., et al. 2013, MNRAS, 435, 999
Di Matteo, T., Springel, V., & Hernquist, L. 2005, Natur, 433, 604
D'Onghia, E., Mapelli, M., & Moore, B. 2008, MNRAS, 389, 1275
Eisenhauer, F., Abuter, R., Bickert, K., et al. 2003, Proc. SPIE, 4841, 1548
Elmegreen, B. G. 2009, in IAU Symp. 254, The Galaxy Disk in Cosmological Context, ed. J. Andersen, J. Bland-Hawthorn, & B. Nordström (Cambridge: Cambridge Univ. Press), 289
Elmegreen, B. G. 2011, in Star Formation in Spiral Arms, ed. C. Charbonnel & T. Montmerle (EAS Publications Series, Vol. 51), 19
Elmegreen, B. G., Bournaud, F., & Elmegreen, D. M. 2008, ApJ, 688, 67
Elmegreen, B. G., Elmegreen, D. M., Fernandez, M. X., & Lemonias, J. J. 2009, ApJ, 692, 12
Elmegreen, D. M., Elmegreen, B. G., & Hirst, A. C. 2004, ApJL, 604, L21
Engel, H., Davies, R. I., Genzel, R., et al. 2010, A&A, 524, 56
Engel, H., Davies, R. I., Genzel, R., et al. 2011, ApJ, 729, 58
Epinat, B., Tasca, L., Amram, P., et al. 2012, A&A, 539, 92
Escala, A., & Larson, R. B. 2008, ApJL, 685, L31
Forbes, J. C., Krumholz, M. R., Burkert, A., & Dekel, A. 2014, MNRAS, 438, 1552
Förster Schreiber, N. M., Genzel, R., Bouché, N., et al. 2009, ApJ, 706, 1364
Förster Schreiber, N. M., Genzel, R., Lehnert, M. D., et al. 2006, ApJ, 645, 1062
Förster Schreiber, N. M., Genzel, R., Newman, S. F., et al. 2013, arXiv:1311.2596
Förster Schreiber, N. M., Shapley, A. E., Erb, D. K., et al. 2011a, ApJ, 731, 65
Förster Schreiber, N. M., Shapley, A. E., Genzel, R., et al. 2011b, ApJ, 739, 45
Foyle, K., Rix, H.-W., Walter, F., & Leroy, A. K. 2010, ApJ, 725, 534
Genel, S., Genzel, R., Bouché, N., et al. 2008, ApJ, 688, 789
Genel, S., Naab, T., Genzel, R., et al. 2012, ApJ, 745, 11
Genzel, R., Burkert, A., Bouché, N., et al. 2008, ApJ, 687, 59
Genzel, R., Lutz, D., Sturm, E., et al. 1998, ApJ, 498, 579
Genzel, R., Newman, S., Jones, T., et al. 2011, ApJ, 733, 101
Genzel, R., Tacconi, L. J., Combes, F., et al. 2012, ApJ, 746, 69
Genzel, R., Tacconi, L. J., Eisenhauer, F., et al. 2006, Natur, 442, 786
Genzel, R., Tacconi, L. J., Gracia-Carpio, J., et al. 2010, MNRAS, 407, 2091
Genzel, R., Tacconi, L. J., Kurk, J., et al. 2013, ApJ, 773, 68
Giavalisco, M., Steidel, C. C., & Macchetto, F. D. 1996, ApJ, 470, 189
Goldreich, P., & Lynden-Bell, D. 1965, MNRAS, 130, 97
Green, A. W., Glazebrook, K., McGregor, P. J., et al. 2010, Natur, 467, 684
Guo, Q., & White, S. D. M. 2008, MNRAS, 384, 2
Grogin, N. A., Kocevski, D. D., Faber, S. M., et al. 2011, ApJS, 197, 35
Heiderman, A., Evans, N. J., II, Allen, L. E., Huard, T., & Heyer, M. 2010, ApJ, 723, 1019
Heyer, M. H., & Brunt, C. M. 2004, ApJL, 615, L45
Hirschmann, M., Naab, T., Davé, R., et al. 2013, MNRAS, 436, 2929
Hitschfeld, M., Kramer, C., Schuster, K. F., Garcia-Burillo, S., & Stutzki, J. 2009, A&A, 495, 795
Hunter, D. A., Elmegreen, B. G., & Baker, A. L. 1998, ApJ, 493, 595
Immeli, A., Samland, M., Gerhard, O., & Westera, P. 2004a, A&A, 413, 547
Immeli, A., Samland, M., Westera, P., & Gerhard, O. 2004b, ApJ, 611, 20
Jones, T. A., Swinbank, A. M., Ellis, R. S., Richard, J., & Stark, D. P. 2010, MNRAS, 404, 1247
Kashino, D., Silverman, J. D., Rodighiero, G., et al. 2013, ApJL, 777, L8
Kauffmann, G., & Haehnelt, M. 2000, MNRAS, 311, 576
Kennicutt, R. C., Jr. 1998a, ApJ, 498, 541
Kennicutt, R. C., Jr. 1998b, ARA&A, 36, 189
Kennicutt, R. C., Jr., Calzetti, D., Walter, F., et al. 2007, ApJ, 671, 333
Kennicutt, R. C., Jr., & Evans, N. J. 2012, ARA&A, 50, 531
Kereš, D., Katz, N., Fardal, M., Davé, R., & Weinberg, D. H. 2009, MNRAS, 395, 160
Kereš, D., Katz, N., Weinberg, D. H., & Davé, R. 2005, MNRAS, 363, 2
Kitzbichler, M. G., & White, S. D. M. 2007, MNRAS, 376, 2
Koekemoer, A. M., Faber, S. M., Ferguson, H. C., et al. 2011, ApJS, 197, 36
Komatsu, E., Smith, K. M., Dunkley, J., et al. 2011, ApJS, 192, 18
Kurk, J., Cimatti, A., Daddi, E., et al. 2013, A&A, 549, A63
Law, D. R., Steidel, C. C., Erb, D. K., et al. 2009, ApJ, 697, 2057
Leroy, A. K., Walter, F., Brinks, E., et al. 2008, AJ, 136, 2782
Leroy, A. K., Walter, F., Sandstrom, K., et al. 2013, AJ, 146, 19
Lilly, S. J., Carollo, C. M., Pipino, A., Renzini, A., & Peng, Y. 2013, ApJ, 772, 119
Magdis, G., Daddi, E., Béthermin, M., et al. 2012, ApJ, 760, 6
Magnelli, B., Saintonge, A., Lutz, D., et al. 2012, A&A, 548, 22
Mancini, C., Förster Schreiber, N. M., Renzini, A., et al. 2011, ApJ, 743, 86
Maraston, C., Pforr, J., Renzini, A., et al. 2010, MNRAS, 407, 830
Martig, M., Bournaud, F., Teyssier, R., & Dekel, A. 2009, ApJ, 707, 250
Martig, M., Crocker, A. F., Bournaud, F., et al. 2013, MNRAS, 432, 1914
Meidt, S. E., Schinnerer, E., García-Burillo, S., et al. 2013, ApJ, 779, 45
Nelson, E. J., van Dokkum, P. G., Brammer, G., et al. 2012, ApJL, 747, L28
Nelson, E. J., van Dokkum, P. G., Momcheva, I., et al. 2013, ApJL, 763, L16
Newman, S. F., Genzel, R., Förster-Schreiber, N. M., et al. 2012, ApJ, 761, 43
Newman, S. F., Genzel, R., Förster-Schreiber, N. M., et al. 2013, ApJ, 767, 104
Noeske, K. G., Weiner, B. J., Faber, S. M., et al. 2007, ApJL, 660, L43
Noguchi, M. 1999, ApJ, 514, 77
Nordon, R., Lutz, D., Saintonge, A., et al. 2013, ApJ, 762, 125
Ocvirk, P., Pichon, C., & Teyssier, R. 2008, MNRAS, 390, 1326
Onodera, S., Kuno, N., Tosaki, T., et al. 2010, ApJL, 722, L127
Puech, M. 2010, MNRAS, 406, 535
Reddy, N. A., Erb, D. K., Pettini, M., Steidel, C. C., & Shapley, A. E. 2010, ApJ, 712, 1070
Rees, M. J., & Ostriker, J. P. 1977, MNRAS, 179, 541
Robertson, B. E., & Bullock, J. S. 2008, ApJL, 685, L27
Robertson, B. E., Bullock, J. S., Cox, T. J., et al. 2006, ApJ, 645, 986
Rodighiero, G., Cimatti, A., Gruppioni, C., et al. 2010, A&A, 518, L25
Rodighiero, G., Daddi, E., Baronchelli, I., et al. 2011, ApJ, 739, 40
Romeo, A. B., & Falstad, N. 2013, MNRAS, 433, 1389
Saintonge, A., Kauffmann, G., Wang, J., et al. 2011, MNRAS, 415, 61
Saintonge, A., Lutz, D., Genzel, R., et al. 2013, ApJ, 778, 2
Saintonge, A., Tacconi, L. J., Fabello, S., et al. 2012, ApJ, 758, 73
Schiminovich, D., Wyder, T. K., Martin, D. C., et al. 2007, ApJS, 173, 315
Schruba, A., Leroy, A. K., Walter, F., Sandstrom, K., & Rosolowsky, E. 2010, ApJ, 722, 1699
Stark, D. P., Swinbank, A. M., Ellis, R. S., et al. 2008, Natur, 455, 775
Swinbank, A. M., Sobral, D., Smail, I., et al. 2012, MNRAS, 426, 935
Tacconi, L. J., Genzel, R., Neri, R., et al. 2010, Natur, 463, 781
Tacconi, L. J., Neri, R., Genzel, R., et al. 2013, ApJ, 768, 74
Toomre, A. 1964, ApJ, 139, 1217
van den Bergh, S., Abraham, R. G., Ellis, R. S., et al. 1996, AJ, 112, 359
Vergani, D., Epinat, B., Contini, T., et al. 2012, A&A, 546, 118
Wang, B., & Silk, J. 1994, ApJ, 427, 759
Whitaker, K. E., van Dokkum, P. G., Brammer, G., & Franx, M. 2012, ApJL, 754, L29
Wisnioski, E., Glazebrook, K., Blake, C., et al. 2012, MNRAS, 422, 3339
Wolfire, M. G., Hollenbach, D., & McKee, C. F. 2010, ApJ, 716, 1191
Wright, S. A., Larkin, J. E., Law, D. R., et al. 2009, ApJ, 699, 421
Wuyts, S., Förster Schreiber, N. M., Genzel, R., et al. 2012, ApJ, 753, 114
Wuyts, S., Förster Schreiber, N. M., Lutz, D., et al. 2011a, ApJ, 738, 106
Wuyts, S., Förster Schreiber, N. M., Nelson, E. J., et al. 2013, ApJ, 779, 135
Wuyts, S., Förster Schreiber, N. M., van der Wel, A., et al. 2011b, ApJ, 742, 96